JGR Solid Earth

RESEARCH ARTICLE
10.1029/2025JB032555

East Meets West: The Trace of the Mesoproterozoic Kibaran Event in the Mantle Lithosphere Beneath Eastern Tanzania

Sheng-Hua Zhou[1,2], Qiao Shu[2,3,4], Sally A. Gibson[5], Hong-Fu Zhang[1], Jing-Jing Zhu[2], Hélène Legros[4], and D. Graham Pearson[4]

[1]Research Center for Earth and Planetary Material Sciences, School of Earth Sciences, Zhejiang University, Hangzhou, China, [2]State Key Laboratory of Critical Mineral Research and Exploration, Institute of Geochemistry, Chinese Academy of Sciences, Guiyang, China, [3]CAS Center for Excellence in Comparative Planetology, Hefei, China, [4]Department of Earth and Atmospheric Sciences, University of Alberta, Edmonton, AB, Canada, [5]Department of Earth Sciences, University of Cambridge, Cambridge, UK

Key Points:

- Lashaine in the Proterozoic Mozambique belt is underlain by typical cratonic mantle
- The lithospheric mantle beneath Lashaine records a major Mesoproterozoic metasomatic event
- The Mesoproterozic metasomatic event has a clear link to the Kibaran event along the western margin of the Tanzanian craton

Supporting Information:

Supporting Information may be found in the online version of this article.

Correspondence to:

Q. Shu,
shuqiao@mail.gyig.ac.cn

Citation:

Zhou, S.-H., Shu, Q., Gibson, S. A., Zhang, H.-F., Zhu, J.-J., Legros, H., & Pearson, D. G. (2026). East meets west: The trace of the Mesoproterozoic Kibaran event in the mantle lithosphere beneath eastern Tanzania. *Journal of Geophysical Research: Solid Earth*, *131*, e2025JB032555. https://doi.org/10.1029/2025JB032555

Received 1 AUG 2025
Accepted 23 DEC 2025

Author Contributions:

Conceptualization: Sheng-Hua Zhou, D. Graham Pearson
Data curation: Sally A. Gibson, Hélène Legros
Funding acquisition: Qiao Shu, Hong-Fu Zhang
Investigation: Sheng-Hua Zhou
Project administration: Qiao Shu, Hong-Fu Zhang
Resources: Jing-Jing Zhu
Supervision: Qiao Shu, Hong-Fu Zhang, D. Graham Pearson
Validation: Sheng-Hua Zhou, Sally A. Gibson
Visualization: Jing-Jing Zhu
Writing – original draft: Sheng-Hua Zhou

Abstract We present elemental geochemistry and multiple isotopic systematics (Re-Os, Lu-Hf, Sm-Nd and Sr) for mantle peridotite xenoliths from Lashaine in northern Tanzania. We use the data to examine how the major Proterozoic tectono-thermal events that affected the crust of the western Tanzanian craton are imprinted on the lithospheric mantle in the Mozambique belt adjacent to the eastern margin of the Tanzanian craton. Whole-rock and mineral compositions together with $^{187}Os/^{188}Os$ ratios of Lashaine peridotites are consistent with Archean-aged cratonic mantle assembled to create the root beneath the Tanzanian cratonic nucleus. Highly radiogenic $^{87}Sr/^{86}Sr$ ratios (0.70411−0.83604), unradiogenic Nd ($\varepsilon Nd = -14 - +2$) and variable Hf isotope ratios ($\varepsilon Hf = +4 - +2{,}912$) of minerals combined with the other geochemical features in Lashaine peridotites reflect extensive melt extraction followed by metasomatic enrichment of the lithospheric mantle by subduction-related melts/fluids. Mineral Lu-Hf isotopic compositions define a 1.4 Ga isochron and, together with the distinctive, robust Lu-Hf model age (1.4 Ga) of one garnet with very high $^{176}Lu/^{177}Hf$ ratio (3.182), indicate that a major Mesoproterozoic subduction-related metasomatic event reset Lu-Hf isotope systematics of the Lashaine peridotites. This over-printing of the mantle lithosphere indicates a clear link to the Mesoproterozoic Kibaran event along the western margin of the Tanzanian craton. We invoke a flat-slab subduction model during the Kibaran event to introduce subduction-related components in a pervasive Mesoproterozoic metasomatic event beneath Lashaine.

Plain Language Summary The Kibaran orogenic event occurred along the western margin of the Tanzanian craton during the Mesoproterozoic and was associated with the amalgamation of the Congo craton and the Tanzanian craton. However, the extent to which this orogenic event affected the lithospheric mantle on the Mozambique belt adjacent to the eastern margin of the Tanzanian craton is less clear, as few studies have focused on the chronological studies on mantle xenoliths in that region. In this study, we use mantle-derived peridotites from Lashaine in northern Tanzania to search for the imprint of the major crustal events that occurred right through the Proterozoic Eon on the lithospheric mantle of the Mozambique belt. We reveal that the lithospheric mantle beneath Lashaine records both an Archean ancestry and later modification closely related to the Mesoproterozoic Kibaran event. An evolution to flat-slab subduction during the Kibaran event may have caused the introduction of subduction-related components into the lower lithosphere at the Mozambique belt, resulting in a pervasive metasomatic overprint in the lithospheric mantle beneath Lashaine.

1. Introduction

The history and processes affecting the accretion of continental masses and the building blocks of supercontinents are largely constrained by crustal geology (e.g., Hofmann, 1988). However, the lithospheric mantle roots underlying these regions can reveal a rich and complex history that tracks the processes involved in continent building and disruption (e.g., Brey & Shu, 2018; Ionov et al., 2015; J. Liu et al., 2021; Pearson et al., 2021; Zhou, Yu, et al., 2023).

The Tanzanian cratonic nucleus has survived for billions of years since its formation (Dawson, 2008). It is bounded to the east by the Mozambique belt, composed of reworked Proterozoic-Archean crust (Maboko, 2000; Möller et al., 1998), and to the southwest by the Ubendian belt (Boniface et al., 2012; Möller et al., 1995). In contrast, post-Archean crustal accretion to the west of the Tanzanian craton is dominated by the Mesoproterozoic

Writing – review & editing: Qiao Shu, Sally A. Gibson, D. Graham Pearson

Kibara and Karagwe-Ankole belts (Figure 1a; Debruyne et al., 2015; Fernandez-Alonso et al., 2012; Tack et al., 2010). These events culminated in the docking of the Congo craton with the Tanzanian craton, forming the larger composite Congo cratonic mass that is underpinned by thick (>150 km) lithospheric mantle (Ritsema et al., 1998; Weeraratne et al., 2003), sandwiching the intervening Kibaran belt at ∼1 Ga, likely during the formation of the Rodinian supercontinent (Debruyne et al., 2015; Villeneuve et al., 2023). However, whether this event triggered deep lithospheric modification extending far beyond the plate boundaries of the Tanzanian craton remains unresolved.

The geodynamic evolution of the Mesoproterozoic "Kibaran" event remains debated. Early models attributed it to prominent bimodal magmatism at ∼1,375 Ma, consisting of a 350 km long zone of mafic and ultramafic, Bushveld-type, layered complexes thought to originate from an enriched lithospheric mantle source in an intracratonic setting; the layered complexes are coeval with voluminous S-type granites (Tack et al., 2010). Recent studies based on integrated geochemical and structural evidence interpreted its formation as related to the collision of the Congo and Tanzanian cratons and emphasized the belt having formed in a subduction-collisional setting (Debruyne et al., 2015; Nambaje et al., 2021). The Kibaran event represents a continent-scale tectonic reorganization, which would be expected to induce craton-scale mantle modification—a phenomenon well-documented in other cratons such as the North China Craton, Slave Craton, Wyoming Craton and Kaapvaal Craton, where subduction processes at cratonic margins have been shown to trigger extensive mantle metasomatism over distances of several hundred kilometers from plate boundaries (Apen et al., 2024; Li, 2020; Weiss et al., 2015; Zhang et al., 2022). Given the scale of the Kibaran event and the width of the Tanzanian craton (∼500 km), similar metasomatic effects could reasonably extend across its entire lithosphere. However, direct evidence for mantle overprints associated with the Kibaran event remains absent. A key outstanding question is the extent to which this major lithospheric disruption along the western margin of the Tanzanian craton is recorded by the numerous samples of mantle xenoliths found in Quaternary volcanic rocks on the Mozambique belt adjacent to the eastern margin of the Tanzanian craton.

In this study, we focus on the Quaternary Lashaine volcano located in the late Proterozoic Mozambique belt in the North Tanzania divergence zone (Dawson, 2008; Mansur et al., 2014; Möller et al., 1998). We use mantle-derived peridotites from the Lashaine volcano to search for the imprint of the major crustal events that occurred right through the Proterozoic Eon on the lithospheric mantle of the Mozambique belt adjacent to the eastern margin of the Tanzanian craton. We develop a further understanding of the metasomatic history affecting the Lashaine peridotites by examining the time-constraints offered by radiogenic isotopes and scrutinizing the trace element compositions of the coexisting clinopyroxenes and orthopyroxenes to better understand the nature of the metasomatic agents. We find that although the Re-Os isotope systematics of the Lashaine peridotites retain the signature of Archean lithosphere formation associated with the genesis of the Tanzanian cratonic nucleus, the Lu-Hf isotope systematics of constituent minerals are dominated by major re-setting associated with metasomatism during the Mesoproterozoic Kibaran event. Our results further demonstrate that subduction processes at craton margins can induce craton-scale lithospheric modification. This finding provides critical insights into supercontinent assembly processes and deep lithospheric dynamics.

2. Geological Setting and Samples

The Tanzanian craton is bounded to the east by a Proterozoic mobile belt, known as the Mozambique belt, and to the southwest by the Ubendian belt. To the west, the Tanzanian craton is bounded by the Kibaran belt (Figure 1a). The Mozambique belt consists of high-grade rocks that were reworked during two separate orogenic events: (a) The Usagaran orogeny that occurred at the southeastern margin of the craton, which may be related to continent-continent collision during the Paleoproterozoic period (∼2 Ga), and led to eclogite-facies metamorphism of a MORB-like precursor (Boniface et al., 2012, 2014; Boniface & Schenk, 2012; Collins et al., 2004; Möller et al., 1995). (b) The East African orogeny (∼600 Ma), which is thought to have formed by the collision between eastern and western Gondwana and led to granulite-facies metamorphism (Fritz et al., 2013). Rocks recording the East African orogeny in the Mozambique belt are dominantly granulites (Figure 1b). Based on protolith ages, metamorphic ages and metamorphic *P-T* paths, the granulite belt is divided into the Western and Eastern Granulites (Apen et al., 2020; Fritz et al., 2009; Mansur et al., 2014). The Eastern Granulites comprise the basement and cover (Figure 1b). Protoliths of the Eastern Granulites formed during the Mesoproterozoic to Neoproterozoic, and were metamorphosed at granulite facies conditions at around 640 Ma (e.g., Apen et al., 2020; Thomas et al., 2013). The Eastern Granulites were accreted outboard of the Western Granulites (Figure 1b).

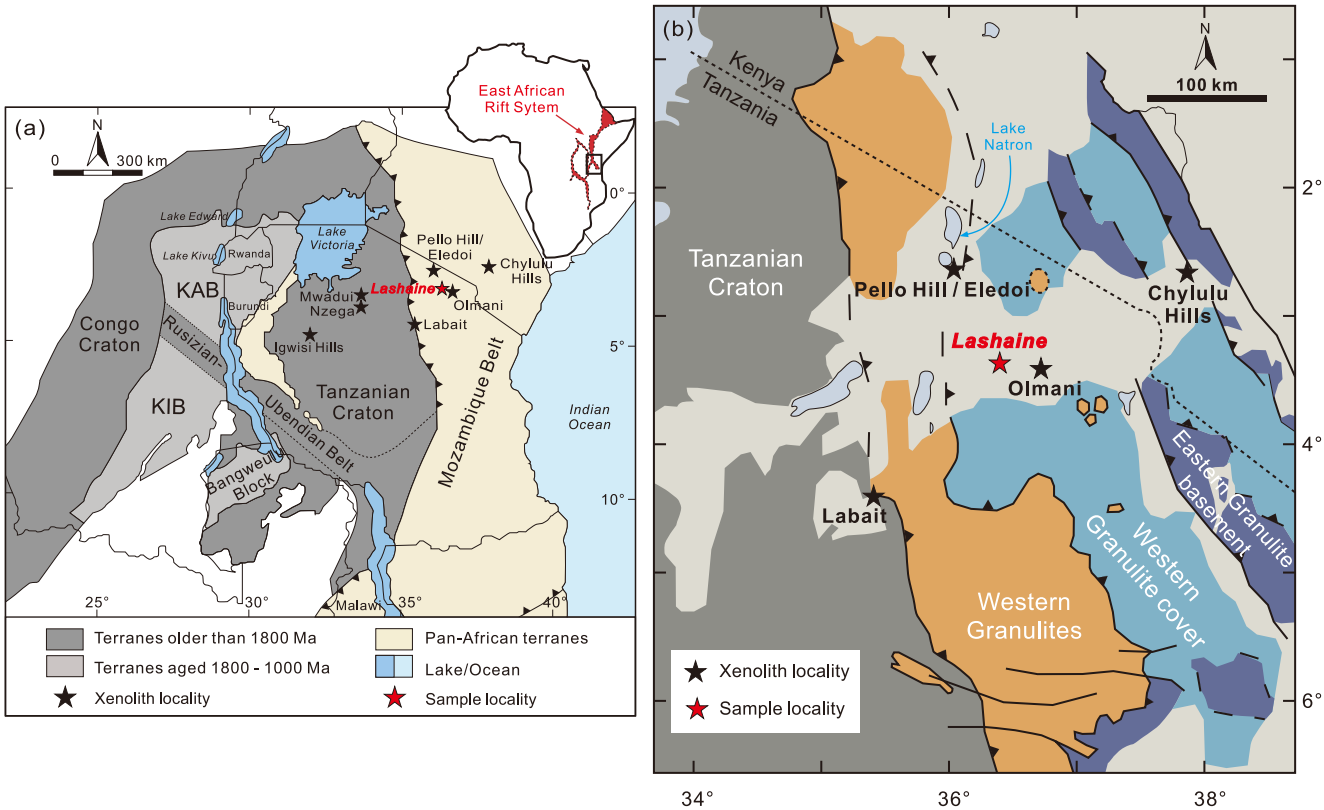

Figure 1. (a) Regional tectonic map of the Tanzanian craton showing the Lashaine xenolith locality (red star), other xenolith-bearing localities (black star) and the surrounding mobile belts (Mozambique belt, Ubendian belt, Karagwe-Ankole belt (KAB) and Kibara belt (KIB). White shaded areas in inset (top right corner) represent the western branch and eastern branch of the East African Rift system. Modified from Dewaele et al. (2011) and Van Daele et al. (2020). (b) Simplified geological map of northern Tanzania showing the xenolith and sample locations (black and red star), Quaternary-Tertiary volcanic rocks and sedimentary cover (light gray), and the distribution of granulites in the Mozambique belt (modified from Apen et al., 2020).

Protoliths of the Western Granulites formed during the Archean, and were metamorphosed at amphibolite-granulite facies conditions at ca. 560−540 Ma (e.g., Apen et al., 2020; Mansur et al., 2014; Sommer et al., 2003; Tenczer et al., 2013; Thomas et al., 2013), that is, later than the Eastern Granulites.

The Kibaran belt forms a NE-SW trending, 1,300 km long, Mesoproterozoic orogenic belt, which separates the Archean-Paleoproterozoic Congo craton from the Archean Tanzanian craton and Paleoproterozoic Bangwuele Block (Figure 1a). The belt was subdivided into two segments, namely, the Karagwe-Ankole belt (KAB) in the northwest and the Kibara belt (KIB) in the southwest, which are separated by the Paleoproterozoic Rusizi-Ubendian belt (Figure 1a). The KAB has two structurally contrasting domains, the Eastern Domain underlain by a Paleoproterozoic basement and the Western Domain with Archean basement (Figure 2a; Nambaje et al., 2020). They are separated by a boundary zone, a NE trending Kabanga-Musongati alignment comprising mafic-ultramafic, Bushveld-type intrusions (Figure 2a; Duchesne et al., 2004; Tack et al., 1994, 2010). The supracrustal cover sequence, namely, the Kagera Supergroup in the Eastern Domain of the KAB is composed of metasedimentary units that overlie the gneissic basement of the Tanzanian craton (Figure 2a; Koegelenberg & Kisters, 2014; Tack et al., 2010). The supracrustal cover sequence of the Akanyaru Supergroup in the Western Domain of the KAB is composed of Mesoproterozoic metasedimentary and subordinate interlayered meta-volcanic rocks, which were intruded by widespread S-type granites and subordinate A-type granites (Figure 2a; De Clercq et al., 2021; Fernandez-Alonso et al., 2012; Nambaje et al., 2021; Tack et al., 2010; Van Daele et al., 2020). The KIB is mainly composed of supracrustal metasedimentary rocks and voluminous granitoid of Mesoproterozoic age, as well as subordinate mafic-intermediate plutonic rocks of Mesoproterozoic age (Figure 2b; Kokonyangi et al., 2004, 2005, 2006). In contrast to the KAB, no A-type granites or mafic-ultramafic layered complexes have been reported in the KIB.

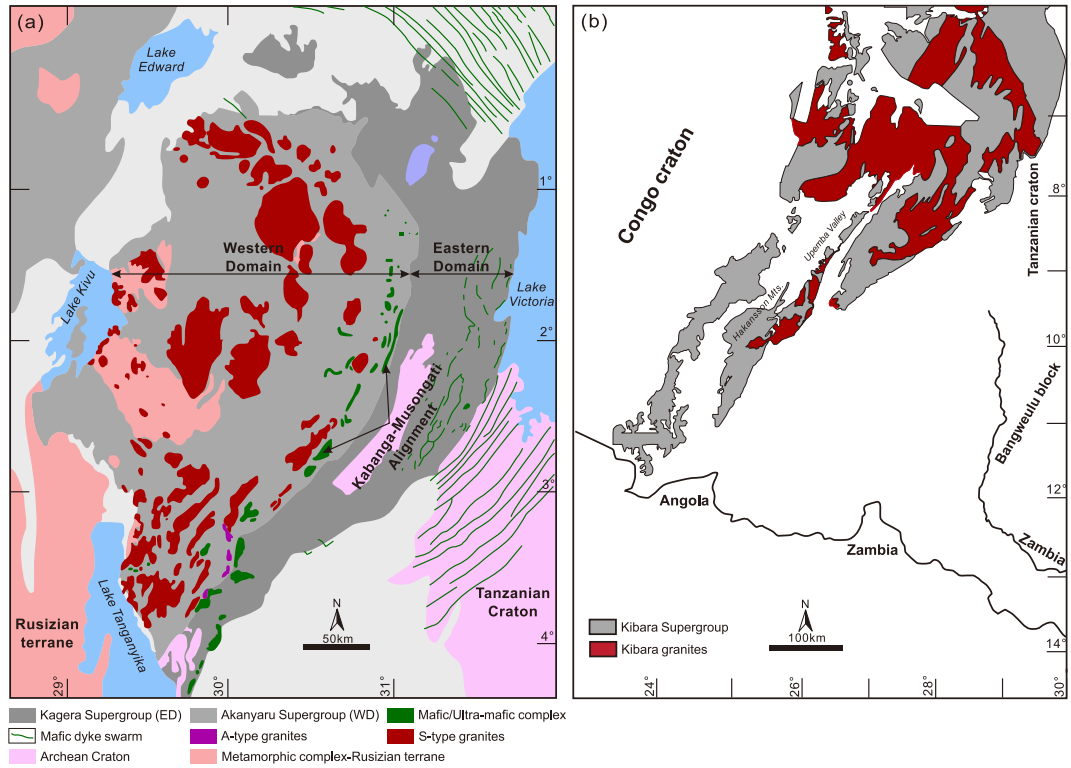

Figure 2. (a) Simplified geological map showing the distribution of Supergroup, mafic/ultra-mafic complex, granites and metamorphic complex in the Karagwe-Ankole belt (modified after Nambaje et al., 2021). (b) Simplified geological map showing the distribution of Supergroup and granites in the Kibara belt (modified after Kokonyangi et al., 2006).

The East African Rift was initiated in the Cenozoic era at ~45 Ma in Ethiopia and propagated southward with time (Rooney, 2017, 2020a, 2020b), forming two branches around the Tanzanian craton: the older, more volcanically active eastern branch and the younger, less active western branch (Figure 1a; Dawson, 1992; Nyblade & Brazier, 2002). The eastern branch propagated into northern Tanzania at ~5 to 8 Ma and continues along the boundary between the Tanzanian craton and Mozambique fold belt (Figure 1a; Dawson, 1992). Geophysical data indicate that the rift may be related to a single or two mantle plumes beneath eastern Africa (Boyce & Cottaar, 2021; Boyce et al., 2021; Civiero et al., 2015; Nyblade et al., 2000; Weeraratne et al., 2003).

The Quaternary Lashaine volcano is located within the late Proterozoic Mozambique belt in the north Tanzania divergence zone, a complex zone of grabens and half grabens (Figure 1; Dawson, 2008; Mansur et al., 2014; Möller et al., 1998). Mantle xenoliths occur within the ankaramitic tuffs of the Lashaine tuff cone (Cohen et al., 1984; Dawson, 2002, 2008; Dawson et al., 1970; Rudnick et al., 1994). Mantle peridotites from Lashaine analyzed in this study were from the J.B. Dawson collection and loaned by the Sedgwick Museum, University of Cambridge. The samples are selected from a suite of peridotites already documented by Gibson et al. (2013) for their petrography and major and trace element compositions (Table 1). The xenolith suite comprises garnet lherzolites and harzburgites, spinel harzburgites, dunite and wehrlite (Table 1). At least two generations of garnet are found in the Lashaine garnet peridotites: (a) ultra-depleted garnets with very low CaO and Cr_2O_3 contents that formed by isochemical exsolution from orthopyroxene (during sub-solidus cooling associated with cratonization) and (b) sub-calcic to calcic garnets with relatively high CaO and low Cr_2O_3 contents that formed by infiltration and reaction of small fraction of carbonatite or silicate melts (metasomatism) (Gibson et al., 2013; their Figure 9). However, the occurrence of ultra-depleted garnets is restricted to specific banded garnet harzburgites (e.g., BD3927 and BD3928; Gibson et al., 2013) derived from shallow lithospheric depths (<125 km), where they form distinct "necklace" textures around orthopyroxene. The garnets analyzed in this study are dominantly calcic to sub-calcic in composition derived from deeper lithospheric levels (e.g., the base of the lithosphere at 125−160 km; Gibson et al., 2013). There is no petrographic and geochemical evidence for mixture of two different generations of garnet in the studied Lashaine peridotites. Based on the MgO and SiO_2 contents of the

Table 1
Modal Abundance and Whole-Rock Abundances of Major Elements Oxides of the Lashaine Peridotite in This Study

Rock type	Sample	Modal abundance (%)					CaO wt.%	Al_2O_3 wt.%	Reference
		Ol	Opx	Cpx	Grt	Sp			
Garnet lherzolite	BD730	64.4	21.5	5.6	8.5		1.45	2.44	Gibson et al. (2013)
Garnet harzburgite	BD740	68.8	21	2	8.2		0.91	2.09	Gibson et al. (2013)
Garnet harzburgite	BD794	70.4	21.4	2.3	5.9		0.87	1.53	Cohen et al. (1984) and Gibson et al. (2013)
Garnet harzburgite cpx-free	BD797	64.4	28.9		4.9	0.4	0.57	1.42	Gibson et al. (2013)
Garnet harzburgite cpx-free	BD775	75	15.9		8.6	0.5	0.42	2.06	Gibson et al. (2013)
Garnet harzburgite cpx-free	BD796	73.9	18.3		6.8		0.59	1.67	Gibson et al. (2013)
Wehrlite (grt-free and sp-free)	BD773	87.9	2.7	9.4			1.74	0.53	Gibson et al. (2013)
Dunite (grt-free)	BD774	91.8	4.7			0.2	0.71	0.24	Gibson et al. (2013)
Spinel harzburgite	BD781	85.7	10.3	3.4		0.6	0.75	0.19	Gibson et al. (2013)
Spinel harzburgite	BD771	87.2	6.8	4.8		0.3	1.58	1.96	Dawson (2002) and Gibson et al. (2013)
Spinel harzburgite cpx-free	BD822	86.3	12.1			0.4	0.31	0.42	Gibson et al. (2013)
Spinel harzburgite cpx-free	BD787	83.8	14.6			0.6	0.25	0.37	Gibson et al. (2013)

Note. Ol: olivine; Cpx: clinopyroxene; Opx: orthopyroxene; Grt: garnet; Sp: spinel.

most refractory spinel peridotites and comparison with the melting model of Herzberg (2004), Gibson et al. (2013) suggested that the Lashaine peridotites represent residues of up to 35% melt extraction. This decompression melting initiated in the garnet stability field and extended to the spinel stability field.

The Re-Os isotope systematics of a sulfide from a single Lashaine mantle xenolith yielded a minimum Re depletion model age (T_{RD}) of 3.4 Ga (Burton et al., 2000) using the primitive upper mantle (PUM) reference model of Meisel et al. (2001). Dawson (2002, 2008) recognized two subsequent episodes of metasomatism in the Lashaine peridotites based on Nd-Pb isotopes. The first occurred at ~2.0 Ga, followed by a more recent metasomatic event, which was deduced from texturally and chemically unequilibrated minerals and involved the addition of K, Ti, Ca, Fe, Nb, and Ta, but without clear age constraints. Here we use the Lu-Hf isotope system to further examine the chronology of lithospheric events because of the generally larger fractionations of Lu from Hf compared to other lithophile-element based parent-daughter isotope pairs (e.g., Wittig et al., 2006); this translates into larger isotopic variability and potentially greater geochronological power in mantle samples (e.g., Shu et al., 2013, 2019).

3. Analytical Methods

Detailed descriptions of the analytical methods used in this study are provided in Text S1 in Supporting Information S1. In-situ major element compositions of garnet were determined by electron probe microanalysis (EPMA, JAX-iHP200F) at the Research Center for Earth and Planetary Material Sciences, School of Earth Sciences, Zhejiang University. These major element concentrations have relative uncertainties typically better than 5%. Trace elements for garnet, clinopyroxene and orthopyroxene were analyzed using laser ablation-inductively coupled plasma-mass spectrometry (LA-ICP-MS) at the State Key Laboratory of Lithospheric Evolution, Institute of Geology and Geophysics, Chinese Academy of Sciences. The analytical accuracy for most trace elements in GOR128-G rock standards was generally better than ±10% (e.g., Wu et al., 2018). The Re-Os isotopic compositions and highly siderophile elements (HSE) concentrations were analyzed both in whole rocks and olivine separates. Rhenium-Os isotope and HSE concentrations were analyzed using an isotope dilution technique coupled with High Pressure Asher (HPA-S, Anton Paar) digestion at the University of Alberta, following the protocols documented in J. Liu and Pearson (2014) and Pearson and Woodland (2000). The Lu-Hf, Sm-Nd and Sr isotopic compositions for minerals were analyzed at the University of Alberta, following procedures detailed in Lazarov et al. (2009) and Shu et al. (2013).

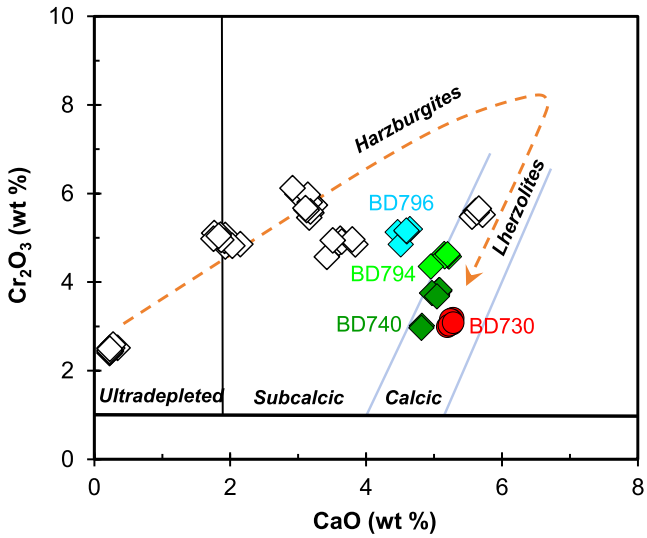

Figure 3. CaO versus Cr_2O_3 diagram for garnets from the Lashaine peridotites (this study and Gibson et al., 2013). The dashed line with an arrow illustrates the general evolutionary trend of Lashaine garnets. The major element compositions of garnet BD796 are from this study, while data for other garnets are from Gibson et al. (2013). Garnet fields are from Grütter et al. (2006).

4. Results

4.1. Major and Trace Element Compositions of Constituent Minerals

In this study, major element compositions of the main constituent minerals were determined from one garnet harzburgite BD796 (not analyzed by Gibson et al., 2013; Table S1). Trace element concentrations in clinopyroxene and orthopyroxene were determined for one garnet lherzolite (BD730) and two garnet harzburgites (BD740 and BD794), and garnet and orthopyroxene compositions (Table S2) were determined from one garnet harzburgite (BD796), to complement the in situ trace element data of minerals from Lashaine samples published by Gibson et al. (2013). In addition, trace element contents of clinopyroxenes and orthopyroxenes from two garnet-free peridotites, one spinel harzburgite (BD781), and one wehrlite (BD773) with relatively high clinopyroxene contents, were also determined in this study (Table S2). With the exception of orthopyroxene, which shows some scatter due to the low concentrations of trace elements, individual analyses of clinopyroxene and garnet in all studied peridotites indicate they are largely homogeneous both within and between grains in each sample (Table S2).

Garnets in the cpx-free garnet harzburgite BD796 have moderate contents of CaO (4.46–4.65 wt%) and Cr_2O_3 (4.85–5.20 wt%; Table S1) and plot within the fields of sub-calcic garnet (Figure 3). In contrast, garnets in Lashaine lherzolite BD730, harzburgites BD740 and BD794 analyzed by Gibson et al. (2013) exhibit high CaO (4.81–5.28 wt%) and low Cr_2O_3 (2.96–4.63 wt%) contents, plotting within the fields of calcic garnet (Figure 3).

Clinopyroxenes have convex-up chondrite normalized rare earth elements (REE) patterns in three garnet peridotites (BD730, BD740 and BD794), the patterns becoming more linear from Tm to Lu (Figure S1 in Supporting Information S1). The calcic garnets in these samples previously analyzed by Gibson et al. (2013) have moderate depletions of light rare earth elements (LREE) or weakly sinusoidal patterns with LREE peaking at Pr, Nd or Sm (Figure S1 in Supporting Information S1). In primitive mantle-normalized diagrams, garnets and clinopyroxenes overall show depletion in Zr and Ti (Figure S1 in Supporting Information S1). Those from garnet peridotites have negative Ti anomalies that tend to be compensated by positive anomalies in their coexisting orthopyroxene (Figure S1 in Supporting Information S1). Sub-calcic garnet from sample BD796 exhibits a strong sinusoidal chondrite-normalized REE pattern with low concentrations of middle rare earth elements (MREE) and high concentrations of LREE and HREE (heavy REE) with LREE peaking at Pr (Figure S1 in Supporting Information S1). Orthopyroxene in sample BD796 shows progressive enrichment from MREE to LREE and nearly flat HREE, characterized by negative Zr anomalies (Figure S1 in Supporting Information S1). Clinopyroxenes in the garnet-free peridotites BD781 and BD773 have convex-up chondrite normalized REE patterns (Figure S1 in Supporting Information S1), coupled with progressive enrichments from HREE to MREE in orthopyroxene (Figure S1 in Supporting Information S1).

We reconstructed the whole-rock compositions for the three garnet peridotites BD730, BD740, and BD794 from the modal abundances and trace element compositions of garnet, clinopyroxene and orthopyroxene. The reconstructed whole-rock compositions overall show weakly sinusoidal chondrite-normalized REE patterns with a continuous decrease from Lu to Dy and a maximum around Nd (Figure 4a). They are enriched in the most incompatible elements but show negative Zr, Hf and Ti anomalies (Figure 4b). The reconstructed whole-rock compositions of garnet peridotite BD796, based on modal abundances and trace element compositions of coexisting garnet and orthopyroxene, exhibits more pronounced sinusoidal REE patterns than those in garnet peridotites BD730, BD740, and BD794 (Figure 4a), characterized by high contents of LREE and HREE, low contents of MREE, and strong negative Zr and Hf anomalies (Figures 4a and 4b). The reconstructed whole-rock compositions of garnet-free peridotites BD781 and BD773 have convex-up chondrite normalized REE patterns (Figure 4c) and show no significant negative anomalies in Zr and Hf (Figure 4d).

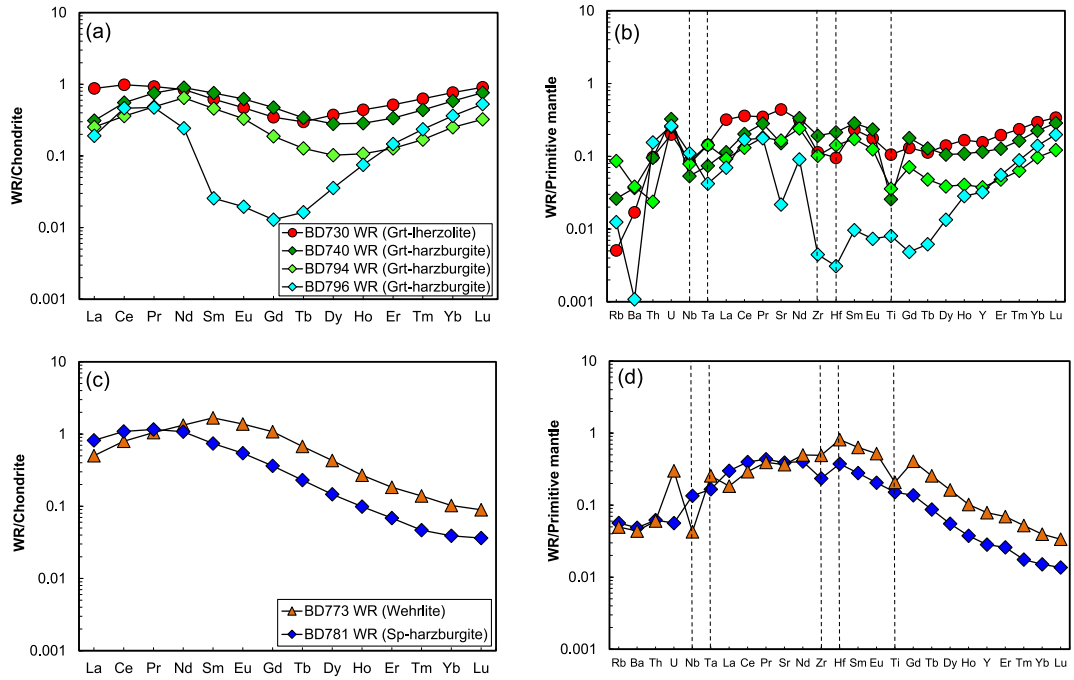

Figure 4. Chondrite-normalized rare earth elements (REE) patterns (a) and primitive mantle-normalized trace element patterns (b) for reconstructed whole-rock (WR) from garnet lherzolites and garnet harzburgites. Chondrite-normalized REE pattern (c) and primitive mantle-normalized trace element patterns (d) for reconstructed WR from wehrlite and spinel harzburgite. The chondrite and primitive mantle compositions are from McDonough and Sun (1995) and Sun and McDonough (1989), respectively. Grt—garnet; Sp—spinel.

4.2. HSE Abundances and Re-Os Isotope Systematics in Whole Rock and Olivine

Whole-rock and/or olivine HSE concentrations and Re-Os isotopic ratios of the Lashaine peridotites are given in Table S3. The PUM-normalized HSE patterns are shown in Figure 5 for garnet-free peridotites, garnet peridotites and for olivine separates. The garnet-free peridotites (except for spinel harzburgite BD771) overall exhibit a significant depletion of platinum-group PGE (PPGE: Pt and Pd) relative to iridium-group PGE (IPGE: Os, Ir and Ru; Figure 5a). The HSE patterns of these samples coincide well with predicted partial melting curves between 30% and 40% partial melting from Becker and Dale (2016) and Lorand et al. (2008). The spinel harzburgite BD771 is distinct in having higher Pd_N/Ir_N (0.23, N refers to PUM-normalized data) compared to predicted partial melting curves (Figure 5a). Two garnet-free peridotites BD771 and BD773 also display obvious Os depletion relative to Ir (Os_N/Ir_N = 0.06−0.15). The garnet peridotites have unfractionated IPGE and negatively sloped, highly fractionated PPGE (Pd_N/Ir_N = 0.01−0.12), creating a normalized HSE pattern that is analogous to those of the garnet-free peridotites (Figure 5b). All peridotites show variable Re enrichment (Re_N/Ir_N = 0.04−1.93; Figures 5a and 5b). The olivine separates in three garnet harzburgites BD775, BD796 and BD797 show similar inter-HSE variations, that is, depletion in Pt and Pd relative to Ir (Pd_N/Ir_N = 0.02−0.04; Figure 5c). They also have significantly lower Os and Ir concentrations (except for sample BD775) relative to the PUM and Os depletion relative to Ir (Os_N/Ir_N = 0.10−0.51; Figure 5c).

The garnet-free peridotites show highly variable $^{187}Re/^{188}Os$ (0.017−0.612) and $^{187}Os/^{188}Os$ ratios (0.1061−0.1255; Figure 6a) relative to the PUM estimates. Two spinel harzburgites (BD822 and BD771) have higher $^{187}Re/^{188}Os$ ratios (0.572 and 0.612) than the PUM (Figure 6a). Among the garnet-free peridotites, spinel harzburgite BD771 has the highest $^{187}Re/^{188}Os$ ratios (0.612) and most radiogenic $^{187}Os/^{188}Os$ ratios (0.1255). The garnet peridotites have lower $^{187}Re/^{188}Os$ (0.022−0.069) and less radiogenic $^{187}Os/^{188}Os$ ratios (0.1103−0.1139) than PUM (Figure 6a). Olivine separates from three garnet harzburgites have comparable $^{187}Re/^{188}Os$ (0.066−0.412) and $^{187}Os/^{188}Os$ ratios (0.1064−0.1115) to the garnet peridotites whereas olivine from sample BD797 has a much higher $^{187}Re/^{188}Os$ ratios (0.412; Figure 6a). There is no relationship between $^{187}Os/^{188}Os$ and $^{187}Re/^{188}Os$ and Pd_N/Ir_N ratios (Figures 6a and 6b). But, for sample BD771, a co-variation exists between $^{187}Os/^{188}Os$ and Pd_N/Ir_N ratios (Figure 6b). The garnet-free peridotites (except for sample BD771) yield

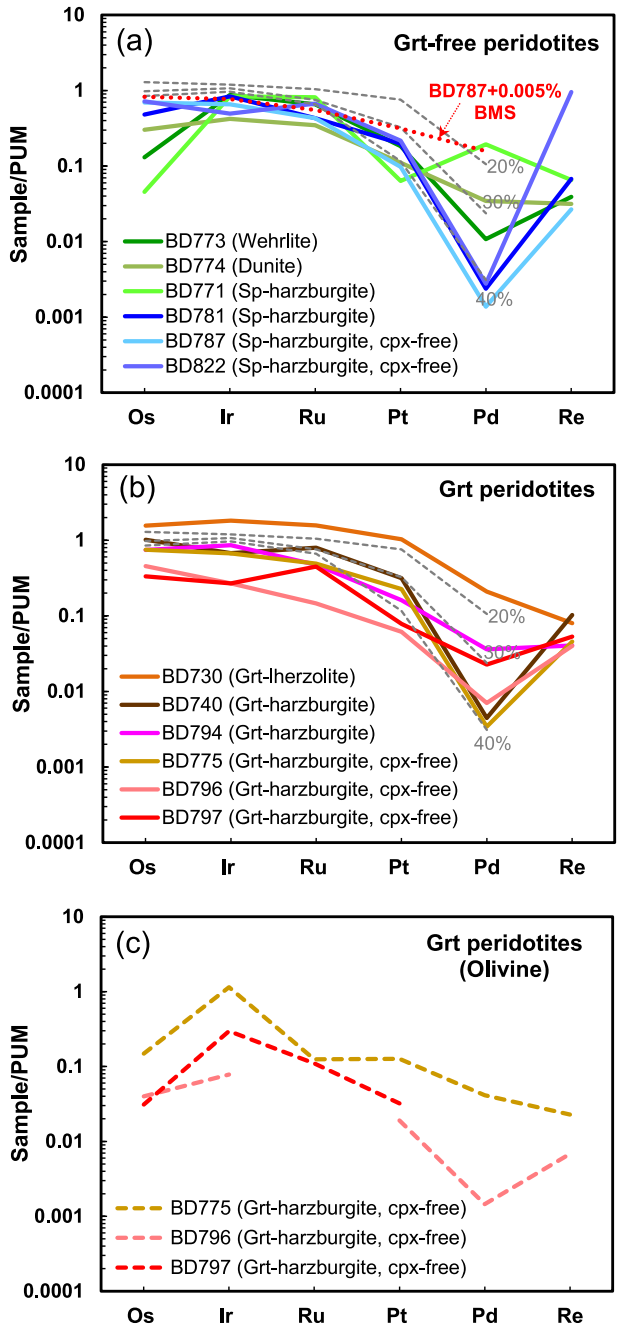

Figure 5. Primitive Upper Mantle (PUM: Becker et al. (2006))-normalized highly siderophile elements (HSE) patterns of Lashaine Grt-free peridotites (a) and Grt peridotites (b). The gray curves in panels (a) and (b) represent the HSE patterns of residual peridotite formed by different degrees of partial melting as given by Becker and Dale (2016) and Lorand et al. (2008). The red dashed line in panel (a) represent the modeled HSE patterns assuming addition of metasomatic base metal sulfides (BMS) to a refractory spinel harzburgite BD787. (c) PUM-normalized HSE patterns for olivine from Lashaine garnet harzburgites. Grt—garnet; Cpx—clinopyroxene; Sp—spinel.

Re depletion model ages (T_{RD}) of 2.8–3.2 Ga (Table S3), whereas spinel harzburgite BD771 has a younger T_{RD} of 0.6 Ga due to its radiogenic $^{187}Os/^{188}Os$ ratios (0.1255). The garnet peridotites have T_{RD} ages from 2.1 to 2.6 Ga (Table S3). The olivine from one garnet harzburgite (BD797) yields a T_{RD} age at 3.1 Ga and the other two have minimum ages of 2.5 and 2.7 Ga (Table S3). Burton et al. (2000) carried out whole-rock analyses of four Lashaine garnet peridotites BD730, BD738, BD-771 and BD-821, with both samples analyzed in duplicate. The Os concentration (0.67−0.86 ppb) and Os isotopic ratios (0.1102−0.1122) reported by Burton et al. (2000) for the same sample BD730 differ significantly from those in this study (Os = 6.10 ppb and $^{187}Os/^{188}Os$ = 0.1139). Although the difference in Os concentration may be explained by the nugget effect related to the heterogeneous distribution of high-Os micro-phases in the whole rock (Pearson et al., 2004), or differences in dissolution technique (e.g., the relatively low-temperature dissolution technique used by Burton et al., 2000), the distinct $^{187}Os/^{188}Os$ ratios are most likely attributed to over-sampling of garnet, which has the most radiogenic Os isotopic composition ($^{187}Os/^{188}Os$ = 0.1205) among all silicate minerals in sample BD730 (Burton et al., 2000). All Lashaine peridotites from our data set, combined with the whole rock and sulfide T_{RD} age data of Burton et al. (2000) share two main T_{RD} age modes at 2.5 Ga and 3.1 Ga (Figure 7).

4.3. Lu-Hf, Sm-Nd, and Sr Isotope Compositions of Garnets and Clinopyroxenes

Garnet from garnet lherzolite BD730, garnet harzburgites BD794 and BD796, and clinopyroxene from spinel harzburgite BD781 were used for Lu-Hf and Sm-Nd isotopic analyses, and the clinopyroxene from sample BD781 was used for Sr isotope determination (Table S4). In addition, Sm-Nd and Sr isotope compositions of clinopyroxenes from two garnet peridotites BD730 and BD794 were also determined in this study (Table S4). The $^{87}Sr/^{86}Sr$ ratios of the clinopyroxenes range from 0.70565 to 0.70690 (Figure 8a), within the much larger range that was previously reported for Lashaine clinopyroxenes by Aulbach et al. (2011) and are much lower than the extremely radiogenic Sr isotopic composition ($^{87}Sr/^{86}Sr > 0.8$) of one Lashaine clinopyroxene reported in Cohen et al. (1984). Furthermore, it is noted that the clinopyroxene in sample BD794 from this study exhibits Sr-Nd isotopic ratios of 0.70565 and 0.51222, which lie outside the analytical uncertainty of the ratios (0.70473 and 0.51253) reported for the same sample by Cohen et al. (1984). This discrepancy likely stems from the analysis of different populations of handpicked mineral separates used for isotopic analysis in the two studies. These populations varied in their mineralogical characteristics, such as the degree of alteration and the presence of mineral inclusions, or other impurities.

The $^{176}Lu/^{177}Hf$ and $^{176}Hf/^{177}Hf$ ratios of garnets and clinopyroxenes vary from 0.001 to 3.182 and from 0.28289 to 0.36512, respectively (εHf from +4 to + 2,912; Figure 8b). Garnet BD796 has the highest $^{176}Lu/^{177}Hf$ ratio (3.182) and most radiogenic $^{176}Hf/^{177}Hf$ ratio (0.36512; εHf = 2,912). Garnets and clinopyroxenes have $^{147}Sm/^{144}Nd$ ratios of 0.021–0.442 and $^{143}Nd/^{144}Nd$ ratios of 0.51194–0.51275, corresponding to εNd from –14 to +2 (Table S4).

Abundances of Lu and Hf obtained by isotopic dilution (ID) and LA-ICP-MS are consisitent (<20% deviations) for the garnet and clinopyroxene from analyzed samples (Figure S2 in Supporting Information S1). However, significant discrepancies between the ID and LA-ICP-MS data exist for Sm and Nd abundances (Figure S3 in Supporting Information S1). Clinopyroxene in

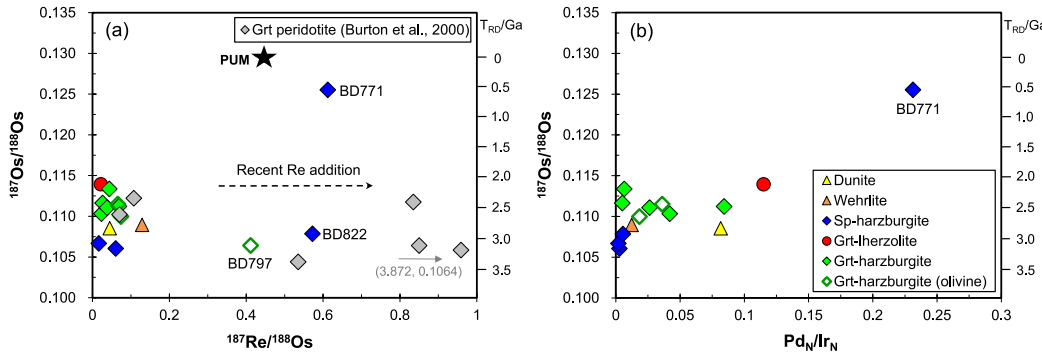

Figure 6. (a) $^{187}Re/^{188}Os$ versus $^{187}Os/^{188}Os$ for the Lashaine peridotites. The composition of primitive upper mantle (PUM) is from Meisel et al. (2001). Panel (a) also shows whole-rock data from garnet peridotites reported by Burton et al. (2000) for comparison. (b) Pd_N/Ir_N versus $^{187}Os/^{188}Os$ for the Lashaine peridotites. Grt—garnet; Sp—spinel.

sample BD781 shows two times higher Sm abundances from LA-ICP-MS than from ID. Similar deviations exist for the Nd abundances of garnet in sample BD796. Clinopyroxene in sample BD781 shows 64% higher Nd abundances for LA-ICP-MS analyses compared to ID. Generally, deviations in the results of the two analytical methods are likely associated with alteration of the mineral rims and the presence of unnoticed mineral inclusions with low Sm and Nd concentrations (e.g., spinel) during handpicking for ID analysis.

Isochron regression of the garnets and clinopyroxenes from samples BD730, BD794, BD796 and BD781 using "Model 3" of IsoplotR (Vermeesch, 2018), for data sets where there is likely significant variation in either the age of re-setting or the initial isotope composition, indicates significant over-dispersion, defining an age of 1,377 ± 118 Ma (dispersion = 0.0017 ± 0.0021; Figure 9) with an initial $^{176}Hf/^{177}Hf$ of 0.2840 ± 0.0028 (εHf = +74). As expected, garnet BD796, with the highest $^{176}Lu/^{177}Hf$ ratio (3.182) and the most radiogenic Hf isotope ratio (0.36512), defines the upper end of the correlation. In contrast, Sm-Nd isotope data for the constituent minerals of the Lashaine peridotites are much more scattered and do not yield any viable regression with age significance (Figure S4 in Supporting Information S1).

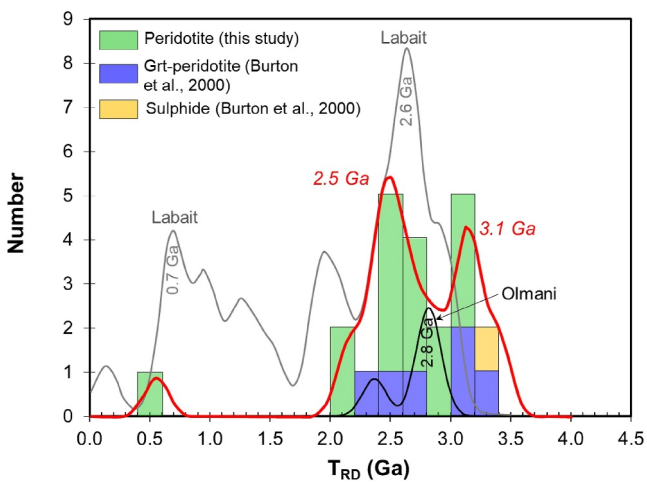

Figure 7. Histogram and probability density curve (red line) for all T_{RD} ages from the Lashaine peridotites, including garnet (Grt) peridotites (both whole rock and olivine separate), garnet-free peridotites and one sulfide from a garnet peridotite (data are compiled from this study and from Burton et al., 2000). Histogram and probability density curve of T_{RD} ages of the Labait peridotites and Olmani peridotites are also shown for comparison (data from Burton et al., 2000; Chesley et al., 1999). The T_{RD} ages of all occurrences are recalculated with the primitive upper mantle reference model (Meisel et al., 2001).

5. Discussion

5.1. History of Melt Depletion of the Lashaine Peridotites

5.1.1. Lithophile and Highly Siderophile Element Evidence

Based on detailed petrography, mineralogy and lithophile element features, Gibson et al. (2013) proposed an evolutional model for the Lashaine peridotites involving initial intensive melt depletion and subsequent metasomatic processes. By examining the MgO-SiO_2 systematics of the spinel-bearing peridotites and applying the melting model of Herzberg (2004), Gibson et al. (2013) deduced that the Lashaine peridotites were formed by up to 35% adiabatic decompression melting of a convecting mantle, with the onset of melting initiated in the garnet stability field and ending in the spinel stability field. The key geochemical evidence for this model is summarized below.

The high Fo contents in some olivines from the Lashaine peridotites strikingly resemble those of olivine inclusions in diamonds from the Mwadui kimberlite pipe, located in the core of the Tanzanian craton (Gibson et al., 2013; their Figure 4). The CaO and Cr_2O_3 contents of garnets in the Lashaine peridotites are comparable to those of garnet megacrysts from the Nzega kimberlite, also from the core of the Tanzanian craton (Gibson et al., 2013; their Figure 7). These features suggest that the composition of lithospheric mantle beneath Lashaine are typical of the cratonic mantle that assembled to create the root beneath the Tanzania cratonic nucleus.

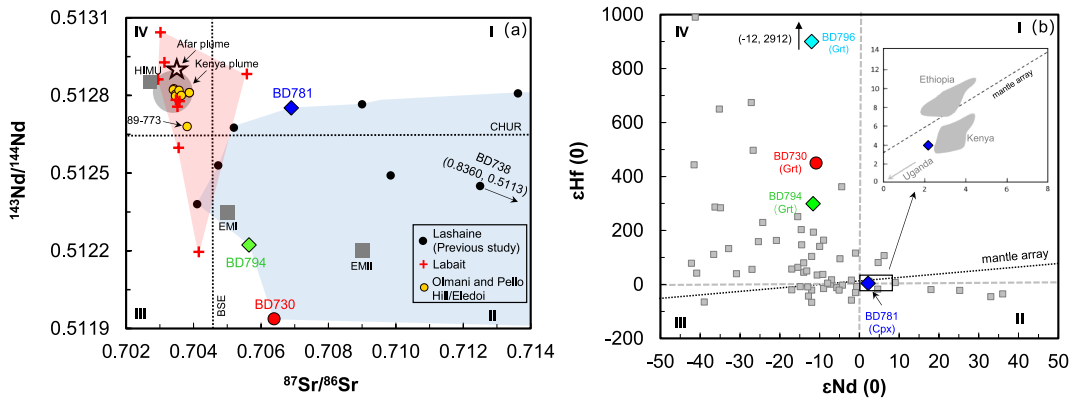

Figure 8. (a) $^{87}Sr/^{86}Sr$ versus $^{143}Nd/^{144}Nd$ diagram for clinopyroxene from Lashaine (this study and Aulbach et al., 2011; Cohen et al., 1984), for clinopyroxene from Labait (Aulbach et al., 2008; Koornneef et al., 2009), and for clinopyroxene and whole-rock from Olmani and Pello Hill/Eledoi (Aulbach et al., 2011; Cohen et al., 1984; Rudnick et al., 1993) in the Tanzanian craton and the Mozambique belt. Whole-rock Sr-Nd isotope ratios from a single monazite-bearing harzburgite 89–773 from Olmani are also shown for comparison (data from Rudnick et al., 1993). The fields for the Afar and Kenya plumes are from Aulbach et al. (2011), Rogers et al. (2000) and Rooney et al. (2012), respectively. Enriched mantle (EMI and EMII) and HIMU mantle end members are from Zindler and Hart (1986). The light blue field encompasses all data from the Lashaine peridotites. The pink field encompasses data from the Labait, Olmani, and Pello Hill/Eledoi peridotites. The sample BD738 is labeled with a black arrow pointing to its position outside the axis range, indicating its highly enriched nature. (b) Present day εHf versus εNd of garnet for garnet lherzolite BD730 and garnet harzburgites BD796 and BD794 from Lashaine and present day εHf versus εNd of clinopyroxene for spinel harzburgite BD781 from Lashaine. The present day εHf and εNd of the subcalcic garnets from the Kaapvaal craton (Lazarov et al., 2009; Shu & Brey, 2015; Shu et al., 2013) are also plotted for comparison (gray boxes). Mantle array is from Vervoort and Blichert-Toft (1999). The fields of Ethiopia, Kenya and Uganda are from Nelson et al. (2019). The Roman numerals (I, II, III, IV) in panels (a) and (b) represent the four different quadrants. Grt—garnet; Cpx—clinopyroxene.

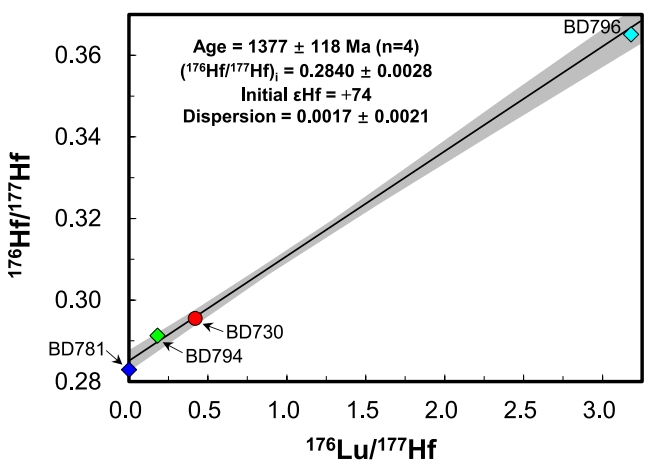

Figure 9. "Model 3" IsoplotR Lu-Hf isochron diagram for garnet and clinopyroxene from the Lashaine peridotites, which define an age of 1.4 Ga with an initial $^{176}Hf/^{177}Hf$ of 0.2840 ± 0.0028 and εHf of +74. Error bars are within the size of the symbols. Uncertainties of $^{176}Lu/^{177}Hf$ ratios are based on replicate standard measurements and are 0.35% (2SE) for garnet and 1% (2SE) for clinopyroxene. Unlike the conventional isochron diagram attributing any over-dispersion to underestimated analytical uncertainties, Model 3 regression of IsoplotR incorporates geological uncertainty through an additional (co)variance term. The parameter "dispersion (x ± y)" in the isochron diagram quantifies isochron scatter, where x represents the excess geological dispersion of the isochron age, and y denotes the absolute analytical uncertainty of x (Vermeesch, 2018).

Highly siderophile elements reside in mantle peridotites predominantly in base metal sulfides (BMS) and platinum-group minerals (Alard et al., 2000; Lorand & Luguet, 2016). Their combined PUM-normalized HSE patterns generally result from partial melting and metasomatic overprint (Ballhaus et al., 2006; Bockrath et al., 2004). Partial melting leaves the relative abundances of the IPGE (Os, Ir and Ru) almost unchanged and increasingly depletes PPGE (Pt and Pd) and Re. This is mainly due to a stronger affinity of PPGE + Re for the sulfide melt and IPGE for refractory sulfide or alloys during incongruent melting of BMS (Luguet & Pearson, 2019; Pearson et al., 2004). The PUM-normalized HSE patterns of residues after various degrees of partial melting from Becker and Dale (2016) and Lorand et al. (2008) are shown in Figures 5a and 5b for reference. The HSE patterns of garnet-free peridotites and garnet peridotites (except for samples BD771 and BD730) coincide with the 30−40% melting patterns (Pd_N/Ir_N < 0.115; Figures 5a and 5b), but their Re contents are strongly increased.

Garnet peridotite BD730 has PPGE-depleted HSE patterns (Figure 5b), which is consistent with <20% melt depletion. However, both Pd and Re contents are elevated in the garnet-free peridotite BD771 compared to the predicted melting curves (Figure 5a). The enrichment of PPGE in the HSE patterns has been observed in many cratonic and off-craton xenoliths from elsewhere (e.g., Kilbourne Hole, New Mexico, Harvey et al., 2015; Letlhakane, Botswana, Luguet et al., 2015; Finsch, South Africa, Shu et al., 2019; Tethyan orogenic belt, Thailand, Zhou, Shu, et al., 2023), as well as in ophiolitic peridotites (e.g., Lesvos, Greece, Xu et al., 2021). Such features are commonly explained by BMS addition to residual peridotite from percolating melts during metasomatic processes (Aulbach et al., 2016; Becker &

Dale, 2016). Because metasomatic BMS are generally enriched in PPGE and Re relative to IPGE (Alard et al., 2000, 2002, 2011), their addition results in a significant elevation in incompatible PPGE on a whole-rock scale. We modeled this as simple mixing of the highly depleted Lashaine peridotite BD787 with a metasomatic BMS. In the absence of equivalent sulfide information from the Lashaine peridotites, metasomatic BMS from garnet peridotite F05JM9 from Finsch on the Kaapvaal craton (Os = 10.4 ppm, Ir = 7.9 ppm, Pt = 33.0 ppm; Pd = 22.2 ppm; Shu et al., 2019) was chosen for modeling the input of metasomatic BMS (i.e., Type 2 BMS) as defined by Alard et al. (2000) and Lorand & Alard. (2001). The enrichment of PPGE (except for Pt) of Lashaine garnet-free peridotite BD771 can be reproduced by the addition of 0.005% F05JM9 BMS (Figure 5a). The variable Pt abundances in this sample may result from selective removal of the Pt-rich microphases through interactions with metasomatic melts (e.g., Ackerman et al., 2009). The olivine separates in three garnet harzburgites BD775, BD796 and BD797 have negatively sloped HSE patterns from Ir to Pd (Pd_N/Ir_N = 0.02−0.04) and low overall abundances (Figure 5c). Such low and variable abundances in olivine separates were also observed in Greenland mantle peridotites by Aulbach et al. (2019). From a comparison with whole-rock compositions, they attributed the variability to an inhomogeneous distribution of sulfides in the olivine separates (nugget effect) and the same may be true here.

5.1.2. Timing of Melt Depletion

High degrees of partial melting result in highly fractionated HSE patterns with low Pd_N/Ir_N and very low Re/Os radios and PUM-like or elevated Os contents in the residue (Pearson et al., 2004). The $^{187}Os/^{188}Os$ ratios in residues with low Re/Os ratios will not significantly evolve with time. The assumption of Re/Os = 0 in combination with the mantle evolution line leads to the concept of the Re depletion age T_{RD} (Walker et al., 1989). Using the measured $^{187}Re/^{188}Os$ ratio gives a Re-Os model age (T_{MA}) that is very susceptible to Re addition or loss during secondary processes. The commonly used T_{RD} model age provides a minimum age for the partial melting event but is also susceptible to ancient Re addition, or the subsequent addition of radiogenic Os. As discussed above, except for garnet-free peridotite BD771, the HSE patterns of the Lashaine peridotites are mainly controlled by melt depletion process. The Lashaine peridotites (except for sample BD771) have low Pd_N/Ir_N, high Os contents and unradiogenic $^{187}Os/^{188}Os$ ratios and fulfill the criteria for partial melting residues. Only Re is strongly elevated (Figure 5). Since their Re/Os ratios are not correlated with $^{187}Os/^{188}Os$ values (Figure 6a), the introduction of Re must be recent, most likely as contamination by the host magma or a precursor rift-related melt, for example, the evidence for recent rift-related metasomatism seen in Labait peridotites from the eastern margin of the Tanzanian craton (Chesley et al., 1999). Their T_{RD} ages are, therefore, the closest estimates of the time of melt depletion underneath Lashaine, even though they are minimum ages. The addition of radiogenic Os is more evident in garnet-free peridotite BD771 due to elevation in both Pd_N/Ir_N and $^{187}Os/^{188}Os$ ratios in this sample (Figure 6b). Therefore, its T_{RD} age is not suitable to estimate the formation age of the lithospheric mantle.

Two main modes in the distribution of T_{RD} ages in the Lashaine peridotites (Figure 7), at 2.5 Ga and 3.1 Ga, can be discerned in a histogram of T_{RD} ages from our data set and the whole rock and sulfide T_{RD} age data of Burton et al. (2000). These authors carried out whole rock analyses of four garnet peridotites, two of them in duplicate. The duplicates of one sample have the oldest T_{RD} age (3.4 Ga), and one further sample has a T_{RD} age of 3.2 Ga. T_{RD} ages for the remaining two samples are spread between 2.4 and 3.1 Ga (Figure 7). One sulfide analyzed by Burton et al. (2000) also yields a T_{RD} age of 3.4 Ga. In summary, the age of 2.5 Ga persists as a minimum estimate for melt depletion of the lithospheric mantle beneath Lashaine though the numerous Mesoarchean ages recorded may be more indicative of the age of depletion of most residues beneath this Archean nucleus. Whatever the actual time of melting, the new and published geochronological data for the Lashaine peridotites suggest that an Archean mantle root is retained beneath the Mozambique belt adjacent to the eastern margin of the Tanzanian craton.

Minimum melt-depletion ages of 2.5 Ga and 3.1 Ga are comparable with the age of overlying crust from the Tanzanian craton nucleus (older than 2.6 Ga; Manya et al., 2006; Manya & Maboko, 2003; Thomas et al., 2016). Moreover, the 2.5 Ga and 3.1 Ga ages are well matched with the granulites exposed in the Mozambique belt. The U-Pb ages of zircon from garnet biotite two-pyroxene granulite at Lashaine are 2.6 Ga, and the whole-rock Nd model ages of biotite-garnet granulites from Lashaine are 2.8 Ga (Apen et al., 2020; Mansur et al., 2014). If the mantle underneath Lashaine is taken as representative of the Tanzanian cratonic mantle, this implies that the Archean root beneath the nucleus of the Tanzania craton dips beneath the Mozambique belt adjacent to the eastern margin of the Tanzanian craton. As discussed in Section 5.1.1, the similarity between Fo values in olivine inclusions in diamonds from Mwadui and those from the Lashaine peridotites (Gibson et al., 2013), as well as the

similarity between CaO and Cr_2O_3 contents in garnet megacrysts from Nzega and those from the Lashaine peridotites (Gibson et al., 2013) suggest that the mantle portion beneath the Mozambique belt and the core of the Tanzanian craton share the similar composition.

By contrast, the peridotites from Labait, to the SW of Lashaine, located in the eastern margin of the Tanzanian cratonic nucleus show T_{RD} age mode of 0.7 Ga and 2.6 Ga (Figure 7; Chesley et al., 1999; Lee & Rudnick, 1999). The presence of the Archean T_{RD} ages in the refractory peridotites beneath Labait attests to the preservation of cratonic mantle beneath Labait, a characterisitic similar to the Lashaine region (Chesley et al., 1999; Lee & Rudnick, 1999). However, the younger T_{RD} age mode evident for the fertile peridotites from Labait is considered to reflect a recent rift-related plume overprint in this region that mixed in radiogenic Os (Chesley et al., 1999; Lee & Rudnick, 1999). Although Archean T_{RD} ages are also evident in the peridotites from Olmani, located within the Mozambique belt, slightly east of Lashaine (Figure 7), many show high $^{187}Re/^{188}Os$ and/or $^{187}Os/^{188}Os$ ratios, indicating that they have been overprinted by the addition of Re and/or radiogenic Os during recent metasomatism, as has been proposed for peridotites at Labait (Burton et al., 2000; Chesley et al., 1999).

5.2. History of Metasomatic Overprinting of the Lashaine Peridotites

5.2.1. Nature and Origin of the Metasomatic Agent

Gibson et al. (2013) demonstrated that the Lashaine garnet peridotites experienced at least two stages of metasomatism. In a plot of olivine Fo content versus modal olivine, garnet peridotites plot off the "oceanic" melting trend of Boyd (1989) indicating silica enrichment and the transformation of some of the olivine to orthopyroxene (Gibson et al., 2013; Rudnick et al., 1994). This metasomatism was suggested to have occurred at an early stage in the evolution of Lashaine lithospheric mantle, pre-dating lithospheric thickening during cratonization. The second type of metasomatism is reflected in the REE patterns of the garnets that range from ultra-depleted garnets with "tick ($\surd$) -shape" REE patterns to sub-calcic garnet with sinusoidal REE patterns and to calcic garnet with weakly sinusoidal patterns (Gibson et al., 2013; their Figure 9). These variations were attributed to a gradual change in the nature of the metasomatic agent from low-temperature high-density fluid (HDF) metasomatism to high-temperature silicate melt-related enrichment on the scale of meters or even kilometers (Gibson et al., 2013). Below, we further constrain the nature of the metasomatic agents in the Lashaine peridotites by scrutinizing the trace element compositions of the coexisting clinopyroxenes and orthopyroxenes.

Calcic garnets in the Lashaine lherzolite BD730 and harzburgites BD740 and BD794 display weakly sinusoidal chondrite-normalized REE patterns, characterized by negative anomalies in Zr, Hf, and Ti (Figure S1 in Supporting Information S1). Based on garnet trace element data, Gibson et al. (2013) attributed these geochemical signatures to infiltration of a high-temperature small-fraction silicate melt. In the garnet peridotite, garnet contributes significantly to the trace element budget of the peridotite, coexisting clinopyroxenes and orthopyroxenes can also host a significant portion of these elements. Reconstructed whole-rock compositions of garnet peridotites BD730, BD740, and BD794 (using coexisting garnets, clinopyroxenes and orthopyroxenes) preserve weakly sinusoidal REE patterns and negative anomalies in Zr, Hf, and Ti (Figures 4a and 4b). Notably, the observed geochemical features are inconsistent with typical silicate melt metasomatism as proposed by Gibson et al. (2013). Although the negative anomalies in Zr, Hf, and Ti could suggest carbonatite metasomatism, the low Zr/Hf ratios (27−44 compared to chondrite value with 36) and low Ca/Al ratios (0.59−0.80) in these samples do not fully agree with the typical characteristics expected for carbonate metasomatism. Given that neither pure silicate melts nor carbonatitic melts can account for the observed geochemical signatures, a metasomatic agent with intermediate composition—most likely a carbonated silicate melt—is suggested, analogous to metasomatic agents documented in garnet peridotites from other cratons (e.g., Aulbach et al., 2013).

Sub-calcic garnet in the cpx-free garnet harzburgite BD796 shows highly sinusoidal REE patterns, characterized by strong negative anomalies in Zr and Hf (Figure S1 in Supporting Information S1). The incorporation of orthopyroxene data into the reconstructed whole-rock compositions of sample BD796 reveals that the negative Zr and Hf anomalies persist even after accounting for the additional contribution from orthopyroxene (Figure 4b). This demonstrates that the observed Zr and Hf anomalies in garnet BD796 are not artifacts resulting from neglecting orthopyroxene contribution, but rather reflects a metasomatic overprint. Compared to other samples in the suite, sample BD796 exhibits more pronounced sinusoidal REE patterns than those in garnet peridotites BD730, BD740, and BD794 (Figure 4a), characterized by high contents of LREE and HREE, low contents of MREE, and strong negative Zr and Hf anomalies (Figures 4a and 4b). These features suggest that the metasomatic

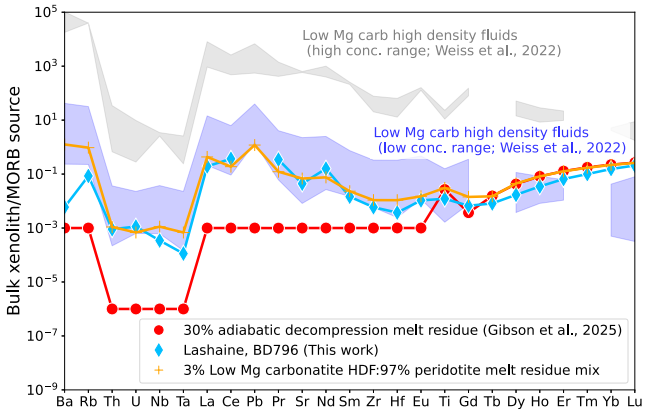

Figure 10. Comparison of trace element patterns for reconstructed whole-rock in Lashaine peridotite BD796 with modeled trace element patterns assuming addition of 3% low-Mg carbonatitic high-density fluids (HDF) from Weiss et al. (2022) to a 30% adiabatic decompression melt residue (Gibson et al., 2025). Data are normalized to the MORB source mantle of Salters and Stracke (2004).

melts/fluids responsible for sample BD796 were poorer in high field strength element (HFSE) with stronger LREE enrichment. Gibson et al. (2013) previously demonstrated that sub-calcic garnets with sinusoidal REE patterns typically occur in low-temperature Lashaine harzburgites derived from shallower depths than the calcic garnets with normal and weakly sinusoidal REE patterns common in lherzolites. Thus, we interpret the systematic variations in chondrite-normalized REE patterns of garnets from Lashaine peridotites as reflecting the compositional continuum of metasomatic agents, resulting from the evolution of a single metasomatic melt through interaction with the lithospheric mantle during ascent (e.g., Aulbach et al., 2013). In such a scenario, carbonated silicate melts that metasomatized samples BD730, BD740, and BD794 may have formed from incipient partial melting of a carbonate-bearing mantle source (e.g., Dasgupta et al., 2006; Foley et al., 2009). Interaction of the deep garnet- and clinopyroxene-bearing lithospheric mantle with such melts could lead to the formation of a residual low-volume carbonatitic fluid that is HFSE-poorer, and strongly enriched in LREE (Aulbach et al., 2013; Stachel et al., 2004), which is able to rise to the shallow lithospheric mantle and produce sinusoidal REE patterns in garnet with which it interacts. Such fluids may also contribute to diamond formation via redox reactions (Stachel & Harris, 2008). Indeed, the highly sinusoidal chondrite-normalized REE patterns—commonly observed in many sub-calcic garnets in cratonic peridotites and garnet inclusions in diamonds—are typically interpreted as resulting from the subsolidus percolation of carbonatitic high-density fluids (HDFs; Stachel et al., 2004; Weiss et al., 2022). Similarly, the sinusoidal chondrite-normalized REE pattern of sub-calcic garnet in sample BD796 falls in the "tick ($\surd$) -shape" category of "ultra-depleted" garnet from Lashaine that Gibson et al. (2013) attribute to minor enrichment by a low-temperature carbonatitic HDFs. For further insights, bulk mixing modeling following the rationale outlined in Gibson et al. (2025) was employed to further assess the effects of carbonatitic HDFs on the trace element compositons of sample BD796. As shown in Figure 10, the trace element patterns for reconstructed whole-rock compositions of sample BD796 (accounting for orthopyroxene contributions) can be reproduced by adding a very small amount (~3%) low-Mg carbonatitic HDFs to a ~30% melt residue.

In garnet-free peridotites, clinopyroxenes and orthopyroxenes dominate the trace element budget of the peridotite, making them critical for reconstructing whole-rock compositions. We therefore analyzed clinopyroxenes and orthopyroxenes from two garnet-free peridotites (spinel harzburgite BD781 and wehrlite BD773). The steeply inclined upward-convex REE patterns of reconstructed whole-rock for wehrlite BD773 (Figure 4c), also reflect a metasomatic overprint. Mantle wehrlites are commonly thought to from by reaction of lherzolite and harzburgite precursors with silica-undersaturated melts (e.g., carbonated silicate melt), which results in high clinopyroxene modes at the expense of orthopyroxene relative to other peridotites in the same xenolith suite (Ionov et al., 2005; Lin et al., 2020; Rudnick et al., 1993; Yaxley et al., 1991). Mineralogical observations in wehrlite BD773 (high modal olivine (88%) and low modal orthopyroxene (3%)) are also consistent with carbonated silicate melt metasomatism. Primitive mantle-normalized trace element patterns for wehrlite BD773 show no significant Zr, Hf, and Ti anomalies (Figure 4d), distinct from those observed in garnet peridotites. This feature could result from interaction with larger melt volumes, where an increasing melt volume result in the dilution of carbonate components by silicate melt and attenuate the geochemical signature typically associated with carbonatitic metasomatism (e.g., Gudfinnsson & Presnall, 2005). Similarly, the reconstructed whole-rock of spinel harzburgite BD781 shows analogous REE patterns (Figures 4c and 4d), implying potential involvement of comparable metasomatic processes despite its distinct modal compositions.

Previous studies have documented that the lithospheric mantle beneath the eastern margin of the Tanzanian craton (e.g., Labait) and adjacent Mozambique belt (e.g., Olmani, Eledoi and Pello Hill) has been overprinted to varying extents by recent rift-related metasomatism associated with plume-derived magmatism (Aulbach et al., 2008, 2011; Chesley et al., 1999; Cohen et al., 1984; Dawson, 2002; Dawson & Smith, 1988; Hui et al., 2015; Koornneef et al., 2009; Rudnick et al., 1993, 1999). Despite the lack of unequivocal evidence linking the trace element signatures of the Lashaine peridotites directly to rift-related magmatism, a relatively recent metasomatic event is also recognized in the Lashaine peridotites based on texturally and chemically unequilibrated minerals

and is interpreted as due to the addition of K, Ti, Ca, Fe, Nb, and Ta (Dawson, 2002). The geochemical signature of this recent event is distinctly different from that of the carbonated silicate melt metasomatism identified in this study. The age of this metasomatism is determined in the following section. These observations suggest that the abundances of certain incompatible trace elements (e.g., Nb, Ta, and Ti) in the Lashaine peridotites may have been overprinted by multistage metasomatism, whereas the major trace element signatures inherited from carbonated silicate melt metasomatism remain largely unaffected by this recent metasomatic event.

The Sr, Nd, and Hf isotope systematics of the Lashaine peridotites can provide further insight into the origin of the metasomatic agent. Clinopyroxenes from Olmani, Pello Hill, and Eledoi are remarkably uniform in their Sr and Nd isotope ratios and entirely overlap with the signature of the plume-related Kenya volcanic rocks (~15 Ma; George et al., 1998; Figure 8a). Aulbach et al. (2011) and Rudnick et al. (1993) attributed the Sr and Nd isotope signatures of peridotites at Olmani to overprinting by recent rift-related carbonatitic melts. The whole-rock analysis of the single monazite-bearing harzburgite 89–773 from Olmani shows similar Sr isotope ratios but significantly lower Nd isotope ratios compared to the clinopyroxene from Olmani peridotite (Figure 8a), which is attributed to recent metasomatism by a carbonatitic melt from a different source (Rudnick et al., 1993). Some clinopyroxenes from Labait plot in this field while three others have higher $^{87}Sr/^{86}Sr$ or lower $^{143}Nd/^{144}Nd$ ratios (pink field in Figure 8a). The peridotite from Labait that overlaps the "plume field" has been interpreted to represent a metasomatic overprint associated with the rift, whereas the three other samples may reflect a metasomatic overprint from an agent from an ancient enriched source such as the lithospheric mantle (Aulbach et al., 2008).

The clinopyroxenes from three Lashaine peridotites in this study and those reported by Aulbach et al. (2011) and Cohen et al. (1984) show highly variable Sr-Nd isotope ratios, mainly plotting within quadrant I and quadrant II in the Sr-Nd isotope diagram (light blue field in Figure 8a), far removed from the Afar and Kenya plume signatures. The present-day εHf and εNd values of garnet and clinopyroxene from the Lashaine peridotites (Figure 8b) are also far from the fields for East African Rift magmatism, as summarized by Nelson et al. (2019). Three peridotites plot in quadrant IV of Figure 8b, and one barely into quadrant I. Residues of partial melting should plot exclusively within the depleted quadrant (I), and for residues of more than 25% partial melting (depending on its age), their εHf values would be up to several thousand and εNd more than +50 (Shu & Brey, 2015). The clinopyroxene and garnet in Lashaine peridotites, for the most part, are displaced from these values because their Lu/Hf and Sm/Nd ratios have been, in most cases, significantly lowered by metasomatism but their Sr-Nd-Hf isotope signatures remain far from those typical of the convecting mantle and indicate clearly that metasomatism at Lashaine is rather ancient, unrelated to Oligocene or younger East African Rift processes (Nelson et al., 2012).

The highly radiogenic $^{87}Sr/^{86}Sr$ ratios (0.70411−0.83604; this study and previous work) and extremely low Rb/Sr ratios in clinopyroxene of the Lashaine peridotites indicate that the carbonate-bearing metasomatic agent must originate from a source with high $^{87}Sr/^{86}Sr$ ratios. Such radiogenic $^{87}Sr/^{86}Sr$ ratios in the metasomatic melt are distinct from those of the depleted mantle (0.7026−0.7027; Carlson & Ionov, 2019; Salters & Stracke, 2004), but overlap values typically associated with an altered oceanic slab (0.70364−0.70744; Staudigel et al., 1995) or marine sediments (>0.706; Plank & Langmuir, 1998), allowing the possibility that the origin of carbonate-bearing metasomatic melts could be related to a subducted slab. This possibility is in-line with high pressure phase equilibria (Thomson et al., 2016) and with the suggestion that the highly variable Sr isotope compositions of the Lashaine peridotite clinopyroxene reflect metasomatism of lithospheric mantle by a slab-derived melt (Aulbach et al., 2011).

Highly radiogenic $^{87}Sr/^{86}Sr$ ratios, coupled with unradiogenic Nd and variable Hf isotope ratios, are also typical for garnets and clinopyroxenes from cratonic peridotites and inclusions in diamonds (e.g., Jacob et al., 1998; Klein-BenDavid & Pearson, 2009; Richardson et al., 1984; Shu & Brey, 2015; Shu et al., 2019; Walker et al., 1989), which suggest that components with ancient subducted, crustal materials were involved. Thus, we infer that the Sr, Nd and Hf isotopic characteristics observed in the Lashaine peridotites reflect the modification of the lithospheric mantle by a highly evolved and enriched component, for example, a melt or fluid derived from a subducted slab.

5.2.2. Timing of Metasomatism

We have demonstrated above that the Sr, Nd and Hf isotope systematics of minerals from the Lashaine peridotites are not related to recent East African Rift processes but reflect an older metasomatic event that affected melt-depleted residues. For a single metasomatic event, peridotite mineral compositions have the potential to form

an isochron and record the time of metasomatism (e.g., J. Liu et al., 2012, 2020; Shu et al., 2013, 2019). However, if the minerals are not cogenetic and the initial isotopic compositions of minerals are not homogenized through a metasomatic event, then far from complete over-printing will not yield useful age information, especially if the system is further disturbed by host-rock interaction.

The Sm-Nd isotopic data of minerals from four Lashaine peridotites show considerable scatter and do not yield any reliable age information (Figure S4 in Supporting Information S1), indicating disturbance of their Sm-Nd isotope systematics. Contamination by host magma is likely one of the main causes, because the host ankaramite has a distinct Nd isotope composition ($^{143}Nd/^{144}Nd = 0.51276$; Cohen et al., 1984) compared to many samples. The Sm-Nd isotopic results in this study are also consistent with many previous studies on mantle xenoliths indicating that Sm-Nd isotope systematics are more susceptible to recent disturbances, or contamination by host magma (e.g., J. Liu et al., 2012, 2020; Shu et al., 2013, 2019). In contrast, the Lu-Hf isotope systematics have the best potential to preserve the geological history of mantle xenoliths, as recorded in peridotites (e.g., J. Liu et al., 2012, 2020; Shu et al., 2013, 2019) and eclogites (e.g., Shu et al., 2014), especially because of the often significant fractionation of Lu from Hf in some minerals such as garnet.

The Hf isotope systematics of garnet from three samples BD730, BD794, and BD796 and clinopyroxene from one sample BD781 vary widely because of their distinct Lu/Hf fractionation. Accepting some over-dispersion of the data due to minor incomplete homogenization of the Hf isotope signatures during metasomatism, they can be regressed using the "Model 3" isochron approach in IsoplotR (Vermeesch, 2018) to yield an isochron age of 1,377 ± 118 Ma (Figure 9), with a highly elevated initial εHf value of +74 that likely reflects, in part, the prior depletion history of these peridotites mixed with a metasomatic agent. No correlation between 1/Hf and $^{176}Hf/^{177}Hf$ is observed for the regressed samples, indicating that the observed correlation cannot be explained as a mixing line. Instead, the Hf isotope systematics indicate almost complete resetting by a major metasomatic event driven by carbonated silicate melt and carbonatitic HDFs on a lithospheric scale, from peridotites residing in the garnet into the spinel stability field. The over-dispersion in the Hf isotopic data in the isochron plot (Figure 9), indicates incomplete equilibration during this event, as frequently experienced by suites of mantle xenoliths that may be separated from each other by meters or even kilometers (Pearson & Wittig, 2014), and seems highly likely if metasomatism took place on a lithospheric scale at Lashaine.

A striking feature in the Lu-Hf isochron correlation defined by the Lashaine peridotites is that BD796 garnet, that defines the most radiogenic Hf isotope composition ($^{176}Hf/^{177}Hf = 0.36512$), anchoring the upper end of this reference isochron (Figure 9) has such a high Lu/Hf ratio and elevated Hf isotopic composition that its Lu-Hf model age is 1.4 Ga (the same as the "model 3" isochron regression), irrespective of which reservoir is chosen as a "model" parent (T_{CHUR} (Hf) = 1,384 Ma; T_{DM}(Hf) = 1,379 Ma). This robustness of the 1.4 Ga model age in garnet BD796 is particularly significant, despite the known challenges arising from the high sensitivity of Hf model ages to Lu-Hf isotopic variations among reference reservoirs (e.g., CHUR vs. DM) and potential post-formation modification of Lu/Hf ratios in the samples. For garnet BD796, the very high $^{176}Lu/^{177}Hf$ ratio (3.182) and radiogenic $^{176}Hf/^{177}Hf$ ratio (0.36512; εHf = 2,912) make it remarkably resistant to later metasomatic disturbances. Furthermore, the extremely high $^{176}Lu/^{177}Hf$ ratios (3.182) produces a steep slope evolution trajectory on the time versus εHf diagram (Figure 11a), minimizing the difference between Hf model ages calculated using different reference reservoirs and resulting in a T_{CHUR} and T_{DM} ages difference for garnet BD796 of 5 Ma. Even when adopting an initial εHf value of +74 (as indicated by the isochron regression) for the starting reservoir, the calculated model age (1,350 Ma) for this garnet remains within 30 Ma of the other model ages and within uncertainty of the isochron age—a robustness attributable to the steep slope of the evolution trajectory. The very high Lu/Hf ratio of garnet BD796 makes it analogous to a phlogopite Rb-Sr model age when the phlogopite has a very high Rb/Sr ratio. Consequently, the ~1.4 Ga Hf model age of garnet BD796 likely provides a good reflection of the timing of metasomatism for garnet BD796 in the Mesoproterozoic, in a peridotite host that experienced melt depletion in the Archean for example, at least 2.5 Ga (T_{RD} age of whole rock from sample BD796 in this study). The metasomatic agent that reset the Hf isotopic systematics of garnet BD796 in this rock was related to the infiltration of carbonatitic HDFs. In other words, this sample has clearly experienced a dramatic fraction of Lu from Hf in Mesoproterozoic times and its model age provides very powerful support for the relevance of the isochron regression age for the broader sample suite. This complex isotopic evolution is illustrated in Figure 11b and discussed further below.

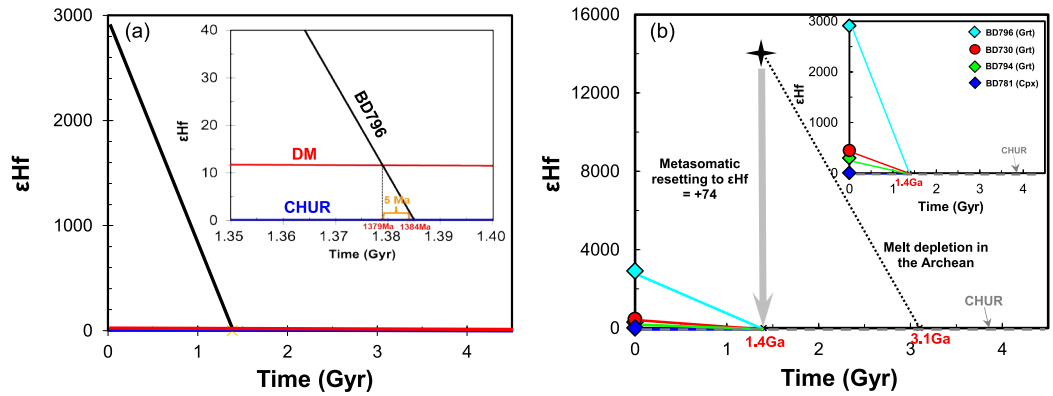

Figure 11. (a) Hf isotope evolution plot illustrating model ages for garnet BD796. (b) The Hf isotopic evolution of garnet and clinopyroxene for the Lashaine peridotites with time, indicating a major Mesoproterozoic re-setting event from a parent with likely Archean heritage. Grt—garnet; Cpx—clinopyroxene.

As discussed in Section 5.2.1, the sinusoidal REE pattern of garnet BD796 is consistent with very low-level enrichment by a highly fractionated, LREE-enriched carbonatitic HDFs, whereas the other three samples (BD730, BD794, and BD781) have reacted with less fractionated carbonated silicate melts and do not, on their own, show such definitive Lu-Hf isotope systematics. The evolution of the carbonated silicate melt that metasomatized peridotites BD730, BD794, and BD781 from the deep lithospheric mantle toward more residual compositions, was accompanied by a increase in Lu/Hf fractionation. In such a scenario, metasomatic melts percolate and react with the deep garnet- and clinopyroxene-bearing lithospheric mantle. This process is accompanied by elemental and isotopic exchange and fractionation between metasomatic melts and peridotite minerals. As the metasomatic melt reacts with wall rocks and accompanying continuous mineral precipitation, a fractionated residual fluid with high LREE/HREE ratios and HFSE depletion will evolve. Such a highly fractionated fluid would continue to migrate upward in the mantle column and would further interact with lithospheric mantle at a shallower depth. The metasomatized garnet thus inherited the trace element features from the highly fractionated residual fluid (e.g., LREE enrichment and HFSE depletion) retaining some characteristics of the residuum, such as a high Lu/Hf ratio, as observed in garnet BD796. By contrast, garnets from samples BD730 and BD794 and clinopyroxenes from sample BD781 have lower $^{176}Lu/^{177}Hf$ ratios and less radiogenic Hf isotopic compositions relative to those from garnet BD796, plotting on the lower end of the 1.4 Ga isochron reference line (Figure 9). As discussed in Section 5.2.1, the different trace element characteristics of these samples are related to the infiltration of less fractionated carbonated silicate melts. Relative to the highly fractionated carbonatitic HFDs, the carbonated silicate melts are higher in HFSE and lower in LREE/HREE ratios, thus resulting in metasomatized samples BD730, BD794, and BD781 having less fractionated Lu/Hf ratios.

The Hf isotopic composition of a highly-depleted melt residue would have been extremely high if evolved over a 1.7 Ga time span (from the occurrence of melt extraction in the Archean (~3.1 Ga) to the occurrence of metasomatic event in the Mesoproterozoic (~1.4 Ga)). We calculate the Hf isotope evolution path for a 1.7 Ga time span, assuming that a mantle source with the CHUR composition experienced 30% fractional melting at 3.1 Ga as indicated by the T_{RD} age mode from this study, which would at least yield an initial εHf value of +14,000 at 1.4 Ga (Figure 11b). Thus, the much lower initial εHf value (+74) indicated by the ~1.4 Ga Hf isotope isochron is the product of mixing between the metasomatic agent and a highly radiogenic peridotitic melting residue (Figure 11b). It is from this base that the variably radiogenic Hf isotope compositions of the minerals in the Lashaine peridotites subsequently developed (Figure 11b).

5.3. Genetic Link Between Mesoproterozoic Metasomatism and the Regional Kibaran Event

The Mesoproterozoic metasomatic age and subduction-related metasomatic signatures identified in the Lashaine peridotites may be placed into the broader context of the evolution of the Tanzanian craton by considering major crustal events. Two distinct orogenic events were recorded in the Mozambique belt to the east of the Tanzanian craton; the ~2.0 Ga Usagaran orogeny and ~600 Ma East African orogeny (Collins et al., 2004; Fritz et al., 2013; Möller et al., 1995). No known crustal events have been identified in the Mozambique belt that would involve the

introduction of subduction-related components in the lithospheric mantle during the Mesoproterozoic era. In contrast, post-Archean crustal accretion to the west of the Tanzanian craton is dominated by the Mesoproterozoic KAB and KIB (Debruyne et al., 2015; Fernandez-Alonso et al., 2012; Tack et al., 2010), as indicated by abundant granitic and mafic-ultramafic magmatism that developed during the Mesoproterozoic era (Figures 1a and 2). For the Kibaran belts, there are currently two main hypotheses concerning their geodynamic evolution. Previous geochronological and geochemical studies have shown that the widespread occurrence of Mesoproterozoic (~1,375 Ma) bimodal mafic-felsic magmatism in the KAB was related to an extensional regime in an intracratonic setting (Tack et al., 2010). Later studies based on structural mapping of the KAB, however, interpreted its formation as related to the collision of the Congo and Tanzanian cratons and emphasized the belt having formed in a collisional setting (Koegelenberg & Kisters, 2014). Moreover, recent geochemical evidence from granites of the KAB further supports the formation in a convergent setting (Nambaje et al., 2021). In contrast, the Mesoproterozoic magmatism of the KIB generally displays arc-like geochemical signatures, interpreted to have occurred in a convergent margin setting due to successive stages of subduction-driven accretion (Debruyne et al., 2015; Kokonyangi et al., 2004, 2005, 2006). In summary, for the KAB and KIB, a convergent margin setting associated with the subduction and collision is favored based on the geochemical and structural evidence.

The Mesoproterozoic (~1.4 Ga) metasomatic ages identified by the Lu-Hf isotope system for the Lashaine peridotites of this study are in good agreement with the timing of the major tectono-magmatic event associated with the Kibaran orogen that formed the KAB and KIB. Thus, it is reasonable to speculate that the Mesoproterozoic metasomatic event affecting the Lashaine peridotites may have been associated with the Kibaran subduction event, occurring at ~1.375 Ga (Tack et al., 2010), in close agreement with the mantle Lu-Hf age. The state and geometry of a subducting slab beneath the Tanzanian craton during the Mesoproterozoic era is poorly constrained. We speculate that the subduction processes involved in the Kibaran event may have extended across the base of the Tanzanian craton, from west to east, disturbing the entire lithosphere.

5.4. Large-Scale Flat-Slab Subduction and Related Metasomatism in the Lithospheric Mantle

The spatial and temporal linkage between the Kibaran event and metasomatic signatures in the lithospheric mantle beneath Lashaine necessitates a mechanism capable of transmitting subduction-related components across the base of the Tanzanian craton. We propose that large-scale flat-slab subduction during the Mesoproterozoic Kibaran event provides a plausible geodynamic framework to reconcile these observations (Figure 12). This hypothesis is supported by (a) geochemical evidence of subduction-derived melts/fluids in the Lashaine peridotites, (b) spatiotemporal correlations between metasomatic ages and Kibaran event, and (c) analogous modern and ancient examples of flat-slab subduction systems.

Flat-slab subduction, characterized by shallow-angle slab descent (≤20°), is a well-documented phenomenon in modern subduction zones (e.g., Axen et al., 2018; Gianni et al., 2023; L. Liu et al., 2021). This process typically generates broad orogenic belts extending from the continental margin into the interior (e.g., Li & Li, 2007). Modern analogs, such as the Pampean flat-slab region in the central Chile, the subducted Nazca plate developed a flat-slab segment (90−110 km depth, 300−600 km inland) between ~11 and 5 Ma (e.g., Marot et al., 2014; Porter et al., 2012). A similar process was observed in the Farallon flat-slab subduction beneath the Western United States, where the subducted Farallon slab maintained a flat geometry (120−150 km depth, >1,500 km inland) from ~90 to 50 Ma (e.g., Axen et al., 2018; Copeland et al., 2017). The most extensive documented case is the South Gondwana flat slab, with a potential inland extent between ~2,280 and 2,600 km (Gianni et al., 2023). Notably, flat slab subduction is not restricted to modern subduction systems and has been a recurrent tectonic process since at least the Mesoproterozoic (Betts et al., 2009), and possibly, a frequent subduction style in the Archean (Abbott et al., 1994). Similar variations in subduction geometry likely affected the subducted slab along the western margin of the Tanzanian craton during the Mesoproterozoic Kibaran event. However, the primary geological evidence crucial for the identification of Kibaran flat-slab subduction events remains exceptionally scarce, likely due to multistage structural destruction and/or poor preservation. Most flat-slab subduction regions are marked by an absence of arc volcanism due to the closure of the hot mantle wedge as the slab flattens beneath the overriding plate (e.g., Axen et al., 2018; Gutscher et al., 2000; X. Liu et al., 2021). This is exemplified by the Tanzanian craton, where the absence of coeval arc magmatism along its eastern margin aligns with flat-slab models predicting either migration cratonward or the complete shut down of magmatic arcs.

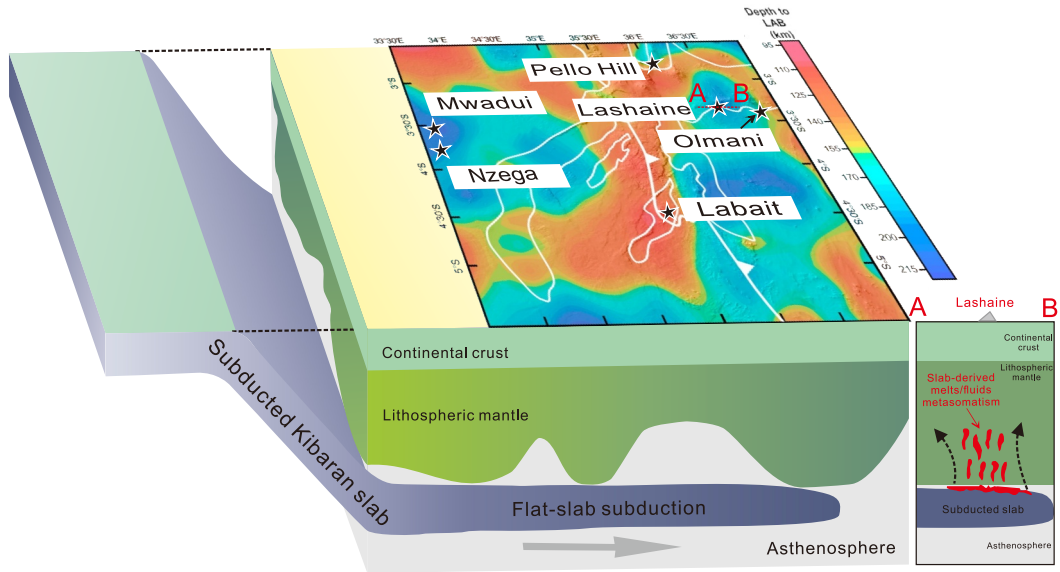

Figure 12. Schematic cartoon showing the metasomatic processes that have affected the lithospheric mantle beneath Lashaine. Flat subduction of the Kibaran slab may have introduced carbonate-bearing crustal components into the base of the lithospheric mantle. Low-degree melting of these components generate carbonated silicate melt (e.g., Dasgupta et al., 2006; Foley et al., 2009), which may infiltrate and metasomatize the overlying lithospheric mantle beneath Lashaine. Gravity data are from Fletcher et al. (2018), which show the presence of thick lithosphere (blue) beneath Lashaine, Mwadui and Nzega. The presence of thick lithosphere is consistent with *P-T* estimates from mantle peridotites found at Lashaine (Gibson et al., 2013). The white line with triangles represents the thrust fault. The red dashed line labeled A–B represents a cross-sectional line through the Lashaine region. The inset in the lower-right corner shows a schematic lithospheric profile and metasomatic processes along cross-section A–B beneath Lashaine.

Plate kinematic reconstructions and seismic tomography studies of modern flat-slab subduction systems reveal that subhorizontal slab geometry facilitates long-distance (over 2,000 km away from the trench) transfer of slab-derived materials into the overriding plate's interior (Gianni et al., 2023), generating significant mantle heterogeneity through interactions between the slab-derived melts/fluids and the base of the cratonic lithosphere. The Laramide orogeny in western North America provides a well-documented example where Farallon flat-slab subduction leads to the formation of fluid-metasomatized mantle xenoliths and lower crustal xenoliths, as well as eclogitic remnants of metamorphosed subducted oceanic crust that are ultimately entrained within Cenozoic basalts (Apen et al., 2024; Lee, 2005; Usui et al., 2003). Farallon flat-slab subduction and the infiltration of slab-derived saline fluids are also suggested as a key mechanism for fluid-rich diamond formation in the central Slave craton (Weiss et al., 2015). In the North China Craton, the flat-slab subduction of the Izanagi plate transported and liberated water beneath the overriding lithosphere (about 600 km from the trench), leading to intense hydration and significant weakening of the cratonic root and further contribute to its thinning and destruction (Li, 2020). In addition, in the Kaapvaal craton, flat-slab subduction may have facilitated the re-healing of cratonic mantle roots by emplacing slab-derived materials into lithospheric gaps left by plume erosion (Zhang et al., 2022). These analogs validate the feasibility of craton-wide metasomatism via flat-slab subduction processes. By analogy, the Kibaran flat-slab subduction along the western margin of the Tanzanian craton may have similarly transported subducted crustal components over distances >500 km inland (Figure 12). Such a process could generate the temperatures and pressures for low-degree melting of subducted crustal components (Gutscher et al., 2000). We proposed that melting of subducted carbonate-bearing Kibaran crust generated carbonated silicate melt (e.g., Dasgupta et al., 2006; Foley et al., 2009), which may infiltrate and metasomatize the overlying lithospheric mantle beneath Lashaine (Figure 12). Further work on mantle xenoliths from other locations on the eastern margin of the Tanzanian craton may be able to better constrain the extent of the link between the metasomatism and the Kibaran event.

6. Conclusion

The elemental geochemistry and multiple isotopic systematics (Re-Os, Lu-Hf, Sm-Nd, and Sr) of the peridotite xenoliths from Lashaine indicate that the lithospheric mantle on the Mozambique belt adjacent to the eastern

margin of the Tanzanian craton represents mantle that assembled to create the root beneath the Tanzania cratonic nucleus. The Lu-Hf isotope system provides very clear documentation of a subsequent widespread enrichment by carbonated silicate melt and carbonaititc HDFs at ∼1.4 Ga. The carbonate-bearing metasomatic agent originated from a source with highly radiogenic $^{87}Sr/^{86}Sr$ ratios, unradiogenic Nd and variable Hf isotopic ratios. These suggest that subduction-related crustal components were involved in the generation of the metasomatic melts. The estimated Lu-Hf isochron age of 1.4 Ga for metasomatism in the lithospheric mantle beneath Lashaine is coeval with the Mesoproterozoic Kibaran event that occurred in the western margin of the Tanzanian craton. To explain these relationships, we invoke a flat-slab subduction model to introduce subduction-related crustal components in a pervasive Mesoproterozoic metasomatic event beneath Lashaine. Thus, the lithospheric mantle in this region records both an Archean ancestry and later modification closely related to major crustal events that occurred right through the Proterozoic Eon on the western margin of the Tanzanian craton, but affecting regions through the craton nucleous.

Conflict of Interest

The authors declare no conflicts of interest relevant to this study.

Data Availability Statement

Text S1 and Figures S1 to S4 in Supporting Information S1. Tables S1, S2, S3 and S4 are available at https://www.scidb.cn/en/s/aeYRji (Zhou et al., 2025).

Acknowledgments
This research was supported by funding from the National Natural Science foundation of China (No. 41973023) and by the Hundred-Talent Program (Chinese Academy of Sciences) (Y8CR001000), China, and by the China Postdoctoral Science Foundation under Grant Number 2024M762800. QS gratefully acknowledges support provided by the "Double First-Class" Academic Masters Gathering Initiative at Zhejiang University. Mantle peridotites from Lashaine are from the JB Dawson collection housed in the Sedgwick Museum, University of Cambridge and curated by SAG. We thank Gerhard P. Brey for constructive comments of an earlier version of the manuscript. We gratefully acknowledge Su-Wen Qiu, Yuan-Yuan Liu, Shi-Tou Wu, Garrett Harris and Sarah Woodland for help in the lab. We also thank Editor Mark Dekkers and Associate Editor for efficient handling, Roberta L. Rudnick and one anonymous reviewer for constructive comments.

References

Abbott, D., Drury, R., & Smith, W. H. F. (1994). Flat to steep transition in subduction style. *Geology*, *22*(10), 937–940. https://doi.org/10.1130/0091-7613(1994)022<0937:FTSTIS>2.3.CO;2

Ackerman, L., Walker, R. J., Puchtel, I. S., Pitcher, L., Jelínek, E., & Strnad, L. (2009). Effects of melt percolation on highly siderophile elements and Os isotopes in subcontinental lithospheric mantle: A study of the upper mantle profile beneath central Europe. *Geochimica et Cosmochimica Acta*, *73*(8), 2400–2414. https://doi.org/10.1016/j.gca.2009.02.002

Alard, O., Griffin, W. L., Lorand, J. P., Jackson, S. E., & O'Reilly, S. Y. (2000). Non-chondritic distribution of the highly siderophile elements in mantle sulphides. *Nature*, *407*(6806), 891–894. https://doi.org/10.1038/35038049

Alard, O., Griffin, W. L., Pearson, N. J., Lorand, J.-P., & O'Reilly, S. Y. (2002). New insights into the Re–Os systematics of sub-continental lithospheric mantle from in situ analysis of sulphides. *Earth and Planetary Science Letters*, *203*(2), 651–663. https://doi.org/10.1016/S0012-821X(02)00799-9

Alard, O., Lorand, J. P., Reisberg, L., Bodinier, J. L., Dautria, J. M., & O'Reilly, S. Y. (2011). Volatile-rich metasomatism in montferrier xenoliths (Southern France): Implications for the abundances of chalcophile and highly siderophile elements in the subcontinental mantle. *Journal of Petrology*, *52*(10), 2009–2045. https://doi.org/10.1093/petrology/egr038

Apen, F. E., Rudnick, R. L., Cottle, J. M., Kylander-Clark, A. R. C., Blondes, M. S., Piccoli, P. M., & Seward, G. (2020). Four-dimensional thermal evolution of the East African Orogen: Accessory phase petrochronology of crustal profiles through the Tanzanian Craton and Mozambique Belt, northeastern Tanzania. *Contributions to Mineralogy and Petrology*, *175*(11), 1–30. https://doi.org/10.1007/s00410-020-01737-6

Apen, F. E., Rudnick, R. L., Flowers, R. M., Gaynor, S. P., & Cottle, J. M. (2024). Metasomatism of the Wyoming craton lower crust during the Laramide orogeny: Extending the record of lithosphere hydration across Western North America. *Earth and Planetary Science Letters*, *641*, 118832. https://doi.org/10.1016/j.epsl.2024.118832

Aulbach, S., Griffin, W. L., Pearson, N. J., & O'Reilly, S. Y. (2013). Nature and timing of metasomatism in the stratified mantle lithosphere beneath the central Slave craton (Canada). *Chemical Geology*, *352*, 153–169. https://doi.org/10.1016/j.chemgeo.2013.05.037

Aulbach, S., Mungall, J. E., & Pearson, D. G. (2016). Distribution and processing of highly siderophile elements in Cratonic Mantle lithosphere. *Reviews in Mineralogy and Geochemistry*, *81*(1), 239–304. https://doi.org/10.2138/rmg.2016.81.5

Aulbach, S., Rudnick, R., & McDonough, W. (2011). Evolution of the lithospheric mantle beneath the East African Rift in Tanzania and its potential signatures in rift magmas. *Geological Society of America Special Paper*, *478*, 105–125. https://doi.org/10.1130/2011.2478(06)

Aulbach, S., Rudnick, R. L., & McDonough, W. F. (2008). Li-Sr-Nd isotope signatures of the plume and cratonic lithospheric mantle beneath the margin of the rifted Tanzanian craton (Labait). *Contributions to Mineralogy and Petrology*, *155*(1), 79–92. https://doi.org/10.1007/s00410-007-0226-4

Aulbach, S., Sun, J., Tappe, S., & Gerdes, A. (2019). Effects of multi-stage rifting and metasomatism on HSE-$^{187}Os/^{188}Os$ systematics of the cratonic mantle beneath SW Greenland. *Contributions to Mineralogy and Petrology*, *174*(2), 1–23. https://doi.org/10.1007/s00410-019-1549-7

Axen, G. J., van Wijk, J. W., & Currie, C. A. (2018). Basal continental mantle lithosphere displaced by flat-slab subduction. *Nature Geoscience*, *11*(12), 961–964. https://doi.org/10.1038/s41561-018-0263-9

Ballhaus, C., Bockrath, C., Wohlgemuth-Ueberwasser, C., Laurenz, V., & Berndt, J. (2006). Fractionation of the noble metals by physical processes. *Contributions to Mineralogy and Petrology*, *152*(6), 667–684. https://doi.org/10.1007/s00410-006-0126-z

Becker, H., & Dale, C. W. (2016). Re–Pt–Os isotopic and highly siderophile element behavior in Oceanic and Continental mantle tectonites. *Reviews in Mineralogy and Geochemistry*, *81*(1), 369–440. https://doi.org/10.2138/rmg.2016.81.7

Becker, H., Horan, M. F., Walker, R. J., Gao, S., Lorand, J. P., & Rudnick, R. L. (2006). Highly siderophile element composition of the Earth's primitive upper mantle: Constraints from new data on peridotite massifs and xenoliths. *Geochimica et Cosmochimica Acta*, *70*(17), 4528–4550. https://doi.org/10.1016/j.gca.2006.06.004

Betts, P. G., Giles, D., Foden, J., Schaefer, B. F., Mark, G., Pankhurst, M. J., et al. (2009). Mesoproterozoic plume-modified orogenesis in eastern Precambrian Australia. *Tectonics*, *28*(3). https://doi.org/10.1029/2008TC002325

Bockrath, C., Ballhaus, C., & Holzheid, A. (2004). Fractionation of the platinum-group elements during mantle melting. *Science*, *305*(5692), 1951–1953. https://doi.org/10.1126/science.1100160

Boniface, N., & Schenk, V. (2012). Neoproterozoic eclogites in the Paleoproterozoic Ubendian Belt of Tanzania: Evidence for a Pan-African suture between the Bangweulu Block and the Tanzania Craton. *Precambrian Research*, *208–211*, 72–89. https://doi.org/10.1016/j.precamres.2012.03.014

Boniface, N., Schenk, V., & Appel, P. (2012). Paleoproterozoic eclogites of MORB-type chemistry and three Proterozoic orogenic cycles in the Ubendian Belt (Tanzania): Evidence from monazite and zircon geochronology, and geochemistry. *Precambrian Research*, *192–195*, 16–33. https://doi.org/10.1016/j.precamres.2011.10.007

Boniface, N., Schenk, V., & Appel, P. (2014). Mesoproterozoic high-grade metamorphism in pelitic rocks of the northwestern Ubendian Belt: Implication for the extension of the Kibaran intra-continental basins to Tanzania. *Precambrian Research*, *249*, 215–228. https://doi.org/10.1016/j.precamres.2014.05.010

Boyce, A., Bastow, I. D., Cottaar, S., Kounoudis, R., Guilloud De Courbeville, J., Caunt, E., & Desai, S. (2021). AFRP20: New P-Wavespeed model for the African mantle reveals two whole-mantle plumes below East Africa and Neoproterozoic modification of the Tanzania craton. *Geochemistry, Geophysics, Geosystems*, *22*(3), e2020GC009302. https://doi.org/10.1029/2020GC009302

Boyce, A., & Cottaar, S. (2021). Insights into deep mantle thermochemical contributions to African magmatism from converted seismic phases. *Geochemistry, Geophysics, Geosystems*, *22*(3), e2020GC009478. https://doi.org/10.1029/2020GC009478

Boyd, F. R. (1989). Compositional distinction between oceanic and cratonic lithosphere. *Earth and Planetary Science Letters*, *96*(1), 15–26. https://doi.org/10.1016/0012-821X(89)90120-9

Brey, G. P., & Shu, Q. (2018). The birth, growth and ageing of the Kaapvaal subcratonic mantle. *Mineralogy and Petrology*, *112*(1), 23–41. https://doi.org/10.1007/s00710-018-0577-8

Burton, K. W., Schiano, P., Birck, J. L., Allègre, C. J., Rehkämper, M., Halliday, A. N., & Dawson, J. B. (2000). The distribution and behaviour of rhenium and osmium amongst mantle minerals and the age of the lithospheric mantle beneath Tanzania. *Earth and Planetary Science Letters*, *183*(1–2), 93–106. https://doi.org/10.1016/S0012-821X(00)00259-4

Carlson, R. W., & Ionov, D. A. (2019). Compositional characteristics of the MORB mantle and bulk silicate earth based on spinel peridotites from the Tariat Region, Mongolia. *Geochimica et Cosmochimica Acta*, *257*, 206–223. https://doi.org/10.1016/j.gca.2019.05.010

Chesley, J. T., Rudnick, R. L., & Lee, C.-T. (1999). Re-Os systematics of mantle xenoliths from the East African Rift: Age, structure, and history of the Tanzanian craton. *Geochimica et Cosmochimica Acta*, *63*(7–8), 1203–1217. https://doi.org/10.1016/S0016-7037(99)00004-6

Civiero, C., Hammond, J. O. S., Goes, S., Fishwick, S., Ahmed, A., Ayele, A., et al. (2015). Multiple mantle upwellings in the transition zone beneath the northern East-African Rift system from relative P-wave travel-time tomography. *Geochemistry, Geophysics, Geosystems*, *16*(9), 2949–2968. https://doi.org/10.1002/2015GC005948

Cohen, R. S., O'Nions, R. K., & Dawson, J. B. (1984). Isotope geochemistry of xenoliths from East Africa: Implications for development of mantle reservoirs and their interaction. *Earth and Planetary Science Letters*, *68*(2), 209–220. https://doi.org/10.1016/0012-821X(84)90153-5

Collins, A. S., Reddy, S. M., Buchan, C., & Mruma, A. (2004). Temporal constraints on Palaeoproterozoic eclogite formation and exhumation (Usagaran Orogen, Tanzania). *Earth and Planetary Science Letters*, *224*(1–2), 175–192. https://doi.org/10.1016/j.epsl.2004.04.027

Copeland, P., Currie, C. A., Lawton, T. F., & Murphy, M. A. (2017). Location, location, location: The variable lifespan of the Laramide orogeny. *Geology*, *45*(3), 223–226. https://doi.org/10.1130/G38810.1

Dasgupta, R., Hirschmann, M. M., & Stalker, K. (2006). Immiscible transition from carbonate-rich to silicate-rich melts in the 3 GPa melting interval of eclogite + CO_2 and genesis of silica-undersaturated ocean island lavas. *Journal of Petrology*, *47*(4), 647–671. https://doi.org/10.1093/petrology/egi088

Dawson, J. B. (1992). Neogene tectonics and volcanicity in the North Tanzania sector of the Gregory Rift Valley: Contrasts with the Kenya sector. *Tectonophysics*, *204*(1–2), 81–92. https://doi.org/10.1016/0040-1951(92)90271-7

Dawson, J. B. (2002). Metasomatism and partial melting in upper-mantle peridotite xenoliths from the Lashaine Volcano, Northern Tanzania. *Journal of Petrology*, *43*(9), 1749–1777. https://doi.org/10.1093/petrology/43.9.1749

Dawson, J. B. (2008). The Gregory rift valley and Neogene-recent volcanoes of northern Tanzania. In *Geological society of London memoir* (Vol. 33, p. 102). https://doi.org/10.1017/S0016756809990288

Dawson, J. B., Powell, D. G., & Reid, A. M. (1970). Ultrabasic xenoliths and lava from the Lashaine volcano, northern Tanzania. *Journal of Petrology*, *11*(3), 519–548. https://doi.org/10.1093/petrology/11.3.519

Dawson, J. B., & Smith, J. V. (1988). Metasomatised and veined upper-mantle xenoliths from Pello Hill, Tanzania: Evidence for anomalously-light mantle beneath the Tanzanian sector of the East African Rift Valley. *Contributions to Mineralogy and Petrology*, *100*(4), 510–527. https://doi.org/10.1007/BF00371380

Debruyne, D., Hulsbosch, N., Van Wilderode, J., Balcaen, L., Vanhaecke, F., & Muchez, P. (2015). Regional geodynamic context for the Mesoproterozoic Kibara Belt (KIB) and the Karagwe-Ankole Belt: Evidence from geochemistry and isotopes in the KIB. *Precambrian Research*, *264*, 82–97. https://doi.org/10.1016/j.precamres.2015.04.001

De Clercq, S., Chew, D., O'Sullivan, G., De Putter, T., De Grave, J., & Dewaele, S. (2021). Characterisation and geodynamic setting of the 1 Ga granitoids of the Karagwe-Ankole belt (KAB), Rwanda. *Precambrian Research*, *356*(1), 106124. https://doi.org/10.1016/j.precamres.2021.106124

Dewaele, S., Henjes-Kunst, F., Melcher, F., Sitnikova, M., Burgess, R., Gerdes, A., et al. (2011). Late Neoproterozoic overprinting of the cassiterite and columbite-tantalite bearing pegmatites of the Gatumba area, Rwanda (Central Africa). *Journal of African Earth Sciences*, *61*(1), 10–26. https://doi.org/10.1016/j.jafrearsci.2011.04.004

Duchesne, J. C., Liégeois, J. P., Deblond, A., & Tack, L. (2004). Petrogenesis of the Kabanga–Musongati layered mafic–ultramafic intrusions in Burundi (Kibaran Belt): Geochemical, Sr–Nd isotopic constraints and Cr–Ni behaviour. *Journal of African Earth Sciences*, *39*(3–5), 133–145. https://doi.org/10.1016/j.jafrearsci.2004.07.055

Fernandez-Alonso, M., Cutten, H., De Waele, B., Tack, L., Tahon, A., Baudet, D., & Barritt, S. D. (2012). The Mesoproterozoic Karagwe-Ankole Belt (formerly the NE Kibara Belt): The result of prolonged extensional intracratonic basin development punctuated by two short-lived far-field compressional events. *Precambrian Research*, *216–219*, 63–86. https://doi.org/10.1016/j.precamres.2012.06.007

Fletcher, A. W., Abdelsalam, M. G., Emishaw, L., Atekwana, E. A., Laó-Dávila, D. A., & Ismail, A. (2018). Lithospheric controls on the rifting of the Tanzanian craton at the Eyasi basin, eastern branch of the East African rift system. *Tectonics*, *37*(9), 2818–2832. https://doi.org/10.1029/2018TC005065

Foley, S. F., Yaxley, G. M., Rosenthal, A., Buhre, S., Kiseeva, E. S., Rapp, R. P., & Jacob, D. E. (2009). The composition of near-solidus melts of peridotite in the presence of CO_2 and H_2O between 40 and 60 kbar. *Lithos*, *112*, 274–283. https://doi.org/10.1016/j.lithos.2009.03.020

Fritz, H., Abdelsalam, M., Ali, K. A., Bingen, B., Collins, A. S., Fowler, A. R., et al. (2013). Orogen styles in the East African Orogen: A review of the Neoproterozoic to Cambrian tectonic evolution. *Journal of African Earth Sciences*, *86*, 65–106. https://doi.org/10.1016/j.jafrearsci.2013.06.004

Fritz, H., Tenczer, V., Hauzenberger, C., Wallbrecher, E., & Muhongo, S. (2009). Hot granulite nappes — Tectonic styles and thermal evolution of the Proterozoic granulite belts in East Africa. *Tectonophysics*, *477*(3–4), 160–173. https://doi.org/10.1016/j.tecto.2009.01.021

George, R., Rogers, N., & Kelley, S. (1998). Earliest magmatism in Ethiopia: Evidence for two mantle plumes in one flood basalt province. *Geology*, *26*(10), 923–926. https://doi.org/10.1130/0091-7613(1998)026<0923:EMIEEF>2.3.CO;2

Gianni, G. M., Likerman, J., Navarrete, C. R., Gianni, C. R., & Zlotnik, S. (2023). Ghost-arc geochemical anomaly at a spreading ridge caused by supersized flat subduction. *Nature Communications*, *14*(1), 2083. https://doi.org/10.1038/s41467-023-37799-w

Gibson, S. A., Jackson, C. J., Crosby, J. C., & Day, J. A. F. (2025). The role of C-O-H-F-Cl fluids in the making of Earth's continental roots. *Nature Communications*, *16*(1), 7842. https://doi.org/10.1038/s41467-025-62888-3

Gibson, S. A., McMahon, S. C., Day, J. A., & Dawson, J. B. (2013). Highly refractory lithospheric mantle beneath the Tanzanian craton: Evidence from lashaine pre-metasomatic garnet-bearing peridotites. *Journal of Petrology*, *54*(8), 1503–1546. https://doi.org/10.1093/petrology/egt020

Grütter, H., Latti, D., & Menzies, A. (2006). Cr-Saturation arrays in concentrate garnet compositions from kimberlite and their use in Mantle barometry. *Journal of Petrology*, *47*(4), 801–820. https://doi.org/10.1093/petrology/egi096

Gudfinnsson, G., & Presnall, D. C. (2005). Continuous gradations among primary carbonatitic, kimberlitic, melilititic, basaltic, picritic, and komatiitic melts in equilibrium with garnet lherzolite at 3–8 GPa. *Journal of Petrology*, *46*(8), 1645–1659. https://doi.org/10.1093/petrology/egi029

Gutscher, M.-A., Maury, R., Eissen, J.-P., & Bourdon, E. (2000). Can slab melting be caused by flat subduction? *Geology*, *28*(6), 535–538. https://doi.org/10.1130/0091-7613(2000)28<535:CSMBCB>2.0.CO;2

Harvey, J., König, S., & Luguet, A. (2015). The effects of melt depletion and metasomatism on highly siderophile and strongly chalcophile elements: S–Se–Te–Re–PGE systematics of peridotite xenoliths from Kilbourne Hole, New Mexico. *Geochimica et Cosmochimica Acta*, *166*, 210–233. https://doi.org/10.1016/j.gca.2015.06.028

Herzberg, C. (2004). Geodynamic information in peridotite petrology. *Journal of Petrology*, *45*(12), 2507–2530. https://doi.org/10.1093/petrology/egh039

Hofmann, A. W. (1988). Chemical differentiation of the Earth: The relationship between mantle, continental crust, and oceanic crust. *Earth and Planetary Science Letters*, *90*(3), 297–314. https://doi.org/10.1016/0012-821X(88)90132-X

Hui, H., Peslier, A., Rudnick, R., Simonetti, A., & Neal, C. (2015). Plume-cratonic lithosphere interaction recorded by water and other trace elements in peridotite xenoliths from the Labait volcano, Tanzania. *Geochemistry, Geophysics, Geosystems*, *16*(6), 1687–1710. https://doi.org/10.1002/2015GC005779

Ionov, D. A., Chanefo, I., & Bodinier, J.-L. (2005). Origin of Fe-rich lherzolites and wehrlites from Tok, SE Siberia by reactive melt percolation in refractory mantle peridotites. *Contributions to Mineralogy and Petrology*, *150*(3), 335–353. https://doi.org/10.1007/s00410-005-0026-7

Ionov, D. A., Doucet, L. S., Carlson, R. W., Golovin, A. V., & Korsakov, A. V. (2015). Post-Archean formation of the lithospheric mantle in the central Siberian craton: Re–os and PGE study of peridotite xenoliths from the Udachnaya kimberlite. *Geochimica et Cosmochimica Acta*, *165*, 466–483. https://doi.org/10.1016/j.gca.2015.06.035

Jacob, D. E., Jagoutz, E., & Sobolev, N. V. (1998). Neodymium and strontium isotopic measurements on single subcalcic garnet grains from Yakutian kimberlites. *Neues Jahrbuch fur Mineralogieu Abhandlungen*, *172*(2–3), 357–379. https://doi.org/10.1127/njma/172/1998/357

Klein-BenDavid, O., & Pearson, D. G. (2009). Origins of subcalcic garnets and their relation to diamond forming fluids—case studies from Ekati (NWT-Canada) and Murowa (Zimbabwe). *Geochimica et Cosmochimica Acta*, *73*(3), 837–855. https://doi.org/10.1016/j.gca.2008.04.044

Koegelenberg, C., & Kisters, A. F. M. (2014). Tectonic wedging, back-thrusting and basin development in the frontal parts of the Mesoproterozoic Karagwe-Ankole belt in NW Tanzania. *Journal of African Earth Sciences*, *97*, 87–98. https://doi.org/10.1016/j.jafrearsci.2014.04.018

Kokonyangi, J., Armstrong, R., Kampunzu, A. B., Yoshida, M., & Okudaira, T. (2004). U–Pb zircon geochronology and petrology of granitoids from Mitwaba (Katanga, Congo): Implications for the evolution of the Mesoproterozoic Kibaran belt. *Precambrian Research*, *132*(1–2), 79–106. https://doi.org/10.1016/j.precamres.2004.02.007

Kokonyangi, J., Kampunzu, A. B., Poujol, M., Okudaira, T., Yoshida, M., & Shabeer, K. P. (2005). Petrology and geochronology of Mesoproterozoic mafic–intermediate plutonic rocks from Mitwaba (D. R. Congo): Implications for the evolution of the Kibaran belt in central Africa. *Geological Magazine*, *142*(1), 109–130. https://doi.org/10.1017/S0016756804009951

Kokonyangi, J. W., Kampunzu, A. B., Armstrong, R., Yoshida, M., Okudaira, T., Arima, M., & Ngulube, D. A. (2006). The Mesoproterozoic kibaride belt (Katanga, SE D.R. Congo). *Journal of African Earth Sciences*, *46*(1–2), 1–35. https://doi.org/10.1016/j.jafrearsci.2006.01.017

Koornneef, J. M., Davies, G. R., Döpp, S. P., Vukmanovic, Z., Nikogosian, I. K., & Mason, P. R. D. (2009). Nature and timing of multiple metasomatic events in the sub-cratonic lithosphere beneath Labait, Tanzania. *Lithos*, *112*, 896–912. https://doi.org/10.1016/j.lithos.2009.04.039

Lazarov, M., Brey, G. P., & Weyer, S. (2009). Time steps of depletion and enrichment in the Kaapvaal craton as recorded by subcalcic garnets from Finsch (SA). *Earth and Planetary Science Letters*, *279*(1–2), 1–10. https://doi.org/10.1016/j.epsl.2008.12.015

Lee, C., & Rudnick, R. (1999). Compositionally stratified cratonic lithosphere: Petrology and geochemistry of peridotite xenoliths from the Labait tuff cone, Tanzania. In *Proceedings of the 7th international Kimberlite conference*. Red Roof Design.

Lee, C. T. A. (2005). Trace element evidence for hydrous metasomatism at the base of the north American lithosphere and possible Association with laramide Low-Angle subduction. *The Journal of Geology*, *113*(6), 673–685. https://doi.org/10.1086/449327

Li, Z.-H. (2020). Flat subduction versus big mantle wedge: Contrasting modes for deep hydration and overriding craton modification. *Journal of Geophysical Research: Solid Earth*, *125*(8), e2020JB020018. https://doi.org/10.1029/2020JB020018

Li, Z.-X., & Li, X.-H. (2007). Formation of the 1300-km-wide intracontinental orogen and postorogenic magmatic province in Mesozoic South China: A flat-slab subduction model. *Geology*, *35*(2), 179–182. https://doi.org/10.1130/G23193A.1

Lin, A.-B., Zheng, J.-P., Aulbach, S., Xiong, Q., Pan, S.-K., & Gerdes, A. (2020). Causes and consequences of wehrlitization beneath a trans-lithospheric fault: Evidence from Mesozoic basalt-borne wehrlite xenoliths from the Tan-Lu fault Belt, North China craton. *Journal of Geophysical Research: Solid Earth*, *125*(7), e2019JB019084. https://doi.org/10.1029/2019JB019084

Liu, J., Carlson, R. W., Rudnick, R. L., Walker, R. J., Gao, S., & Wu, F.-Y. (2012). Comparative sr–nd–hf–os–pb isotope systematics of xenolithic peridotites from Yangyuan, North China Craton: Additional evidence for a Paleoproterozoic age. *Chemical Geology*, *332–333*, 1–14. https://doi.org/10.1016/j.chemgeo.2012.09.013

Liu, J., & Pearson, D. G. (2014). Rapid, precise and accurate Os isotope ratio measurements of nanogram to sub-nanogram amounts using multiple Faraday collectors and amplifiers equipped with 1012 Ω resistors by N-TIMS. *Chemical Geology*, *363*, 301–311. https://doi.org/10.1016/j.chemgeo.2013.11.008

Liu, J., Pearson, D. G., Shu, Q., Sigurdsson, H., Thomassot, E., & Alard, O. (2020). Dating Post-Archean lithospheric mantle: Insights from Re-Os and Lu-Hf isotopic systematics of the Cameroon Volcanic Line peridotites. *Geochimica et Cosmochimica Acta*, *278*, 177–198. https://doi.org/10.1016/j.gca.2019.07.010

Liu, J., Pearson, D. G., Wang, L. H., Mather, K. A., Kjarsgaard, B. A., Schaeffer, A. J., et al. (2021). Plume-driven recratonization of deep continental lithospheric mantle. *Nature*, *592*(7856), 732–736. https://doi.org/10.1038/s41586-021-03395-5

Liu, L., Liu, L., & Xu, Y.-G. (2021). Mesozoic intraplate tectonism of East Asia due to flat subduction of a composite terrane slab. *Earth-Science Reviews*, *214*, 103505. https://doi.org/10.1016/j.earscirev.2021.103505

Liu, X., Currie, C. A., & Wagner, L. S. (2021). Cooling of the continental plate during flat-slab subduction. *Geosphere*, *18*(1), 49–68. https://doi.org/10.1130/GES02402.1

Lorand, J. P., & Alard, O. (2001). Platinum-group element abundances in the upper mantle: New constraints from in situ and whole-rock analyses of Massif Central xenoliths (France). *Geochimica et Cosmochimica Acta*, *65*(16), 2789–2806. https://doi.org/10.1016/S0016-7037(01)00627-5

Lorand, J. P., & Luguet, A. (2016). Chalcophile and siderophile elements in mantle rocks: Trace elements controlled by trace minerals. *Reviews in Mineralogy and Geochemistry*, *81*(1), 441–488. https://doi.org/10.2138/rmg.2016.81.08

Lorand, J. P., Luguet, A., & Alard, O. (2008). Platinum-Group elements: A new set of key tracers for the Earth's interior. *Elements*, *4*(4), 247–252. https://doi.org/10.2113/GSELEMENTS.4.4.247

Luguet, A., Behrens, M., Pearson, D. G., König, S., & Herwartz, D. (2015). Significance of the whole rock Re–Os ages in cryptically and modally metasomatised cratonic peridotites: Constraints from HSE–Se–Te systematics. *Geochimica et Cosmochimica Acta*, *164*, 441–463. https://doi.org/10.1016/j.gca.2015.06.016

Luguet, A., & Pearson, G. (2019). Dating mantle peridotites using Re-Os isotopes: The complex message from whole rocks, base metal sulfides, and platinum group minerals. *American Mineralogist*, *104*(2), 165–189. https://doi.org/10.2138/am-2019-6557

Maboko, M. A. H. (2000). Nd and Sr isotopic investigation of the Archean–Proterozoic boundary in north eastern Tanzania: Constraints on the nature of Neoproterozoic tectonism in the Mozambique Belt. *Precambrian Research*, *102*(1–2), 87–98. https://doi.org/10.1016/S0301-9268(00)00060-7

Mansur, A. T., Manya, S., Timpa, S., & Rudnick, R. L. (2014). Granulite-Facies xenoliths in rift basalts of Northern Tanzania: Age, composition and origin of Archean lower crust. *Journal of Petrology*, *55*(7), 1243–1286. https://doi.org/10.1093/petrology/egu024

Manya, S., Kobayashi, K., Maboko, M. A. H., & Nakamura, E. (2006). Ion microprobe zircon U–Pb dating of the late Archaean metavolcanics and associated granites of the Musoma-Mara Greenstone Belt, Northeast Tanzania: Implications for the geological evolution of the Tanzania Craton. *Journal of African Earth Sciences*, *45*(3), 355–366. https://doi.org/10.1016/j.jafrearsci.2006.03.004

Manya, S., & Maboko, M. A. H. (2003). Dating basaltic volcanism in the Neoarchaean Sukumaland Greenstone Belt of the Tanzania Craton using the Sm–Nd method: Implications for the geological evolution of the Tanzania Craton. *Precambrian Research*, *121*(1–2), 35–45. https://doi.org/10.1016/S0301-9268(02)00195-X

Marot, M., Monfret, T., Gerbault, M., Nolet, G., Ranalli, G., & Pardo, M. (2014). Flat versus normal subduction zones: A comparison based on 3-D regional traveltime tomography and petrological modelling of central Chile and western Argentina (29°–35°S). *Geophysical Journal International*, *199*(3), 1633–1654. https://doi.org/10.1093/gji/ggu355

McDonough, W. F., & Sun, S. S. (1995). The composition of the Earth. *Chemical Geology*, *120*(3–4), 223–253. https://doi.org/10.1016/0009-2541(94)00140-4

Meisel, T., Walker, R. J., Irving, A. J., & Lorand, J. P. (2001). Osmium isotopic compositions of mantle xenoliths: A global perspective. *Geochimica et Cosmochimica Acta*, *65*(8), 1311–1323. https://doi.org/10.1016/S0016-7037(00)00566-4

Möller, A., Mezger, K., & Schenk, V. (1998). Crustal Age domains and the evolution of the Continental crust in the Mozambique Belt of Tanzania: Combined Sm–Nd, Rb–Sr, and Pb–Pb isotopic evidence. *Journal of Petrology*, *39*(4), 749–783. https://doi.org/10.1093/petroj/39.4.749

Möller, A., Appel, P., Mezger, K., & Schenk, V. (1995). Evidence for a 2 Ga subduction zone: Eclogites in the Usagaran belt of Tanzania. *Geology*, *23*(12), 1067–1070. https://doi.org/10.1130/0091-7613(1995)023<1067:EFAGSZ>2.3.CO;2

Nambaje, C., Satish-Kumar, M., Williams, I. S., Takahashi, T., & Sajeev, K. (2021). Granitic rocks from Rwanda: Vital clues to the tectonic evolution of the Karagwe–Ankole Belt. *Lithos*, *404–405*, 106490. https://doi.org/10.1016/j.lithos.2021.106490

Nambaje, C., Williams, I. S., Satish-Kumar, M., & Sajeev, K. (2020). Direct evidence for Archean crust in the Western Domain of the Karagwe Ankole Belt, Rwanda: Implications for Neoarchean to Paleoproterozoic crustal evolution. *Precambrian Research*, *350*, 105851. https://doi.org/10.1016/j.precamres.2020.105851

Nelson, W. R., Furman, T., van Keken, P. E., Shirey, S. B., & Hanan, B. B. (2012). Os-Hf isotopic insight into mantle plume dynamics beneath the East African Rift System. *Chemical Geology*, *320–321*, 66–79. https://doi.org/10.1016/j.chemgeo.2012.05.020

Nelson, W. R., Hanan, B. B., Graham, D. W., Shirey, S. B., Yirgu, G., Ayalew, D., & Furman, T. (2019). Distinguishing plume and metasomatized lithospheric Mantle contributions to post-flood basalt volcanism on the Southeastern Ethiopian Plateau. *Journal of Petrology*, *60*(5), 1063–1094. https://doi.org/10.1093/petrology/egz024

Nyblade, A. A., & Brazier, R. A. (2002). Precambrian lithospheric controls on the development of the East African rift system. *Geology*, *30*(8), 755–758. https://doi.org/10.1130/0091-7613(2002)030<0755:PLCOTD>2.0.CO;2

Nyblade, A. A., Owens, T. J., Gurrola, H., Ritsema, J., & Langston, C. A. (2000). Seismic evidence for a deep upper mantle thermal anomaly beneath east Africa. *Geology*, *28*(7), 599–602. https://doi.org/10.1130/0091-7613(2000)28<599:SEFADU>2.0.CO;2

Pearson, D. G., Irvine, G. J., Ionov, D. A., Boyd, F. R., & Dreibus, G. E. (2004). Re–Os isotope systematics and platinum group element fractionation during mantle melt extraction: A study of massif and xenolith peridotite suites. *Chemical Geology*, *208*(1–4), 29–59. https://doi.org/10.1016/j.chemgeo.2004.04.005

Pearson, D. G., Scott, J. M., Liu, J., Schaeffer, A., Wang, L. H., van Hunen, J., et al. (2021). Deep continental roots and cratons. *Nature*, *596*(7871), 199–210. https://doi.org/10.1038/s41586-021-03600-5

Pearson, D. G., & Wittig, N. (2014). The formation and evolution of cratonic mantle lithosphere–evidence from mantle xenoliths. *Treatise on Geochemistry*, *3*, 255–292. https://doi.org/10.1016/B978-0-08-095975-7.00205-9

Pearson, D. G., & Woodland, S. J. (2000). Solvent extraction/anion exchange separation and determination of PGEs (Os, Ir, Pt, Pd, Ru) and Re–Os isotopes in geological samples by isotope dilution ICP-MS. *Chemical Geology*, *165*(1), 87–107. https://doi.org/10.1016/S0009-2541(99)00161-8

Plank, T., & Langmuir, C. H. (1998). The chemical composition of subducting sediment and its consequences for the crust and mantle. *Chemical Geology*, *145*(3–4), 325–394. https://doi.org/10.1016/S0009-2541(97)00150-2

Porter, R., Gilbert, H., Zandt, G., Beck, S., Warren, L., Calkins, J., et al. (2012). Shear wave velocities in the Pampean flat-slab region from Rayleigh wave tomography: Implications for slab and upper mantle hydration. *Journal of Geophysical Research*, *117*(B11), B11301. https://doi.org/10.1029/2012JB009350

Richardson, S. H., Gurney, J. J., Erlank, A. J., & Harris, J. W. (1984). Origin of diamonds in old enriched mantle. *Nature*, *310*(5974), 198–202. https://doi.org/10.1038/310198a0

Ritsema, J., Nyblade, A. A., Owens, T. J., Langston, C. A., & VanDecar, J. C. (1998). Upper mantle seismic velocity structure beneath Tanzania, east Africa: Implications for the stability of cratonic lithosphere. *Journal of Geophysical Research*, *103*(B9), 21201–21213. https://doi.org/10.1029/98JB01274

Rogers, N., Macdonald, R., Fitton, J. G., George, R., Smith, M., & Barreiro, B. (2000). Two mantle plumes beneath the East African rift system: Sr, Nd and Pb isotope evidence from Kenya Rift basalts. *Earth and Planetary Science Letters*, *176*(3–4), 387–400. https://doi.org/10.1016/S0012-821X(00)00012-1

Rooney, T. O., Hanan, B. B., Graham, D. W., Furman, T., Blichert-Toft, J., & Schilling, J.-G. (2012). Upper mantle pollution during Afar plume–continental rift interaction. *Journal of Petrology*, *53*(2), 365–389. https://doi.org/10.1093/petrology/egr065

Rooney, T. O. (2017). The Cenozoic magmatism of East-Africa: Part I—Flood basalts and pulsed magmatism. *Lithos*, *286–287*, 264–301. https://doi.org/10.1016/j.lithos.2017.05.014

Rooney, T. O. (2020a). The Cenozoic magmatism of East Africa: Part II – Rifting of the mobile belt. *Lithos*, *360–361*, 105291. https://doi.org/10.1016/j.lithos.2019.105291

Rooney, T. O. (2020b). The Cenozoic magmatism of East Africa: Part III–Rifting of the craton. *Lithos*, *360–361*, 105390. https://doi.org/10.1016/j.lithos.2020.105390

Rudnick, R. L., Ireland, T. R., Gehrels, G., Irving, A. J., Chesley, J. T., & Hanchar, J. M. (1999). Dating mantle metasomatism: U-pb geochronology of zircons in cratonic mantle xenoliths from Montana and Tanzania. In J. J. Gurney, J. L. Gurney, M. D. Pascoe, & S. H. Richardson (Eds.), *The Nixon volume, proc. Seventh int. Kimberlite conf* (pp. 728–735).

Rudnick, R. L., McDonough, W. F., & Chappell, B. W. (1993). Carbonatite metasomatism in the northern Tanzanian mantle: Petrographic and geochemical characteristics. *Earth and Planetary Science Letters*, *114*(4), 463–475. https://doi.org/10.1016/0012-821X(93)90076-L

Rudnick, R. L., McDonough, W. F., & Orpin, A. (1994). Northern Tanzanian peridotite xenoliths: A comparison with Kaapvaal peridotites and inferences on metasomatic interactions. In H. O. A. Meyer & O. Leonardos (Eds.), *Kimberlites, related rocks and mantle xenoliths*, *Proceedings fifth int. Kimb. Conf.* (Vol. 1, pp. 336–353). C.P.R.M.

Salters, V. J. M., & Stracke, A. (2004). Composition of the depleted mantle. *Geochemistry, Geophysics, Geosystems*, *5*(5), Q05B07. https://doi.org/10.1029/2003GC000597

Shu, Q., & Brey, G. P. (2015). Ancient mantle metasomatism recorded in subcalcic garnet xenocrysts: Temporal links between mantle metasomatism, diamond growth and crustal tectonomagmatism. *Earth and Planetary Science Letters*, *418*, 27–39. https://doi.org/10.1016/j.epsl.2015.02.038

Shu, Q., Brey, G. P., Gerdes, A., & Hoefer, H. E. (2013). Geochronological and geochemical constraints on the formation and evolution of the mantle underneath the Kaapvaal craton: Lu–hf and Sm–Nd systematics of subcalcic garnets from highly depleted peridotites. *Geochimica et Cosmochimica Acta*, *113*, 1–20. https://doi.org/10.1016/j.gca.2013.03.010

Shu, Q., Brey, G. P., Gerdes, A., & Hoefer, H. E. (2014). Mantle eclogites and garnet pyroxenites – The meaning of two-point isochrons, Sm–Nd and Lu–Hf closure temperatures and the cooling of the subcratonic mantle. *Earth and Planetary Science Letters*, *389*, 143–154. https://doi.org/10.1016/j.epsl.2013.12.028

Shu, Q., Brey, G. P., Pearson, D. G., Liu, J., Gibson, S. A., & Becker, H. (2019). The evolution of the Kaapvaal craton: A multi-isotopic perspective from lithospheric peridotites from Finsch diamond mine. *Precambrian Research*, *331*, 105380. https://doi.org/10.1016/j.precamres.2019.105380

Sommer, H., Kröner, A., Hauzenberger, C., Muhongo, S., & Wingate, M. T. D. (2003). Metamorphic petrology and zircon geochronology of high-grade rocks from the central Mozambique Belt of Tanzania: Crustal recycling of Archean and Palaeoproterozoic material during the Pan-African orogeny. *Journal of Metamorphic Geology*, *21*(9), 915–934. https://doi.org/10.1111/j.1525-1314.2003.00491.x

Stachel, T., Aulbach, S., Brey, G. P., Harris, J. W., Leost, I., Tappert, R., & Viljoen, K. S. (2004). The trace element composition of silicate inclusions in diamonds: A review. *Lithos*, *77*(1), 1–19. https://doi.org/10.1016/j.lithos.2004.03.027

Stachel, T., & Harris, J. W. (2008). The origin of cratonic diamonds—Constraints from mineral inclusions. *Ore Geology Reviews*, *34*(1), 5–32. https://doi.org/10.1016/j.oregeorev.2007.05.002

Staudigel, H., Davies, G. R., Hart, S. R., Marchant, K. M., & Smith, B. M. (1995). Large scale isotopic Sr, Nd and O isotopic anatomy of altered oceanic crust: DSDP/ODP sites417/418. *Earth and Planetary Science Letters*, *130*(1–4), 169–185. https://doi.org/10.1016/0012-821X(94)00263-X

Sun, S. S., & McDonough, W. F. (1989). Chemical and isotopic systematics of oceanic basalts: Implications for mantle composition and processes. *Geological Society, London, Special Publications*, *42*(1), 313–345. https://doi.org/10.1144/GSL.SP.1989.042.01.19

Tack, L., Liégeois, J. P., Deblond, A., & Duchesne, J. C. (1994). Kibaran A-type granitoids and mafic rocks generated by two mantle sources in a late orogenic setting (Burundi). *Precambrian Research*, *68*(3–4), 323–356. https://doi.org/10.1016/0301-9268(94)90036-1

Tack, L., Wingate, M. T. D., De Waele, B., Meert, J., Belousova, E., Griffin, B., et al. (2010). The 1375 Ma "Kibaran event" in Central Africa: Prominent emplacement of bimodal magmatism under extensional regime. *Precambrian Research*, *180*(1–2), 63–84. https://doi.org/10.1016/j.precamres.2010.02.022

Tenczer, V., Hauzenberger, C., Fritz, H., Hoinkes, G., Muhongo, S., & Klötzli, U. (2013). Crustal age domains and metamorphic reworking of the deep crust in Northern-Central Tanzania: A U/Pb zircon and monazite age study. *Mineralogy and Petrology*, *107*(5), 679–707. https://doi.org/10.1007/s00710-012-0210-1

Thomas, R. J., Roberts, N. M. W., Jacobs, J., Bushi, A. M., Horstwood, M. S. A., & Mruma, A. (2013). Structural and geochronological constraints on the evolution of the eastern margin of the Tanzania Craton in the Mpwapwa area, central Tanzania. *Precambrian Research*, *224*, 671–689. https://doi.org/10.1016/j.precamres.2012.11.010

Thomas, R. J., Spencer, C., Bushi, A. M., Baglow, N., Boniface, N., de Kock, G., et al. (2016). Geochronology of the central Tanzania Craton and its southern and eastern orogenic margins. *Precambrian Research*, *277*, 47–67. https://doi.org/10.1016/j.precamres.2016.02.008

Thomson, A. R., Walter, M. J., Kohn, S. C., & Brooker, R. A. (2016). Slab melting as a barrier to deep carbon subduction. *Nature*, *529*(7584), 76–79. https://doi.org/10.1038/nature16174

Usui, T., Nakamura, E., Kobayashi, K., Maruyama, S., & Helmstaedt, H. (2003). Fate of the subducted Farallon plate inferred from eclogite xenoliths in the Colorado Plateau. *Geology*, *31*(7), 589–592. https://doi.org/10.1130/0091-7613(2003)031<0589:FOTSFP>2.0.CO;2

Van Daele, J., Hulsbosch, N., Dewaele, S., & Muchez, P. (2020). Metamorphic and metasomatic evolution of the Western Domain of the Karagwe-Ankole Belt (Central Africa). *Journal of African Earth Sciences*, *165*, 103783. https://doi.org/10.1016/j.jafrearsci.2020.103783

Vermeesch, P. (2018). IsoplotR: A free and open toolbox for geochronology. *Geoscience Frontiers*, *9*(5), 1479–1493. https://doi.org/10.1016/j.gsf.2018.04.001

Vervoort, J. D., & Blichert-Toft, J. (1999). Evolution of the depleted mantle: Hf isotope evidence from juvenile rocks through time. *Geochimica et Cosmochimica Acta*, *63*(3), 533–556. https://doi.org/10.1016/S0016-7037(98)00274-9

Villeneuve, M., Gärtner, A., Kalikone, C., & Wazi, N. (2023). Amalgamation in the Central African Shield (CAS) by the Kibaran orogen: New hypothesis and implications for the Rodinia assembly. *Journal of African Earth Sciences*, *202*, 104936. https://doi.org/10.1016/j.jafrearsci.2023.104936

Walker, R. J., Carlson, R. W., Shirey, S. B., & F.R, B. (1989). Os, Sr, Nd, and Pb isotope systematics of southern African peridotite xenoliths: Implications for the chemical evolution of subcontinental mantle. *Geochimica et Cosmochimica Acta*, *53*(7), 1583–1595. https://doi.org/10.1016/0016-7037(89)90240-8

Weeraratne, D. S., Forsyth, D. W., Fischer, K. M., & Nyblade, A. A. (2003). Evidence for an upper mantle plume beneath the Tanzanian craton from Rayleigh wave tomography. *Journal of Geophysical Research*, *108*(B9), 2427. https://doi.org/10.1029/2002JB002273

Weiss, Y., Czas, J., & Navon, O. (2022). Fluid inclusions in fibrous diamonds. *Reviews in Mineralogy and Geochemistry*, *88*(1), 475–532. https://doi.org/10.2138/rmg.2022.88.09

Weiss, Y., McNeill, J., Pearson, D. G., Nowell, G. M., & Ottley, C. J. (2015). Highly saline fluids from a subducting slab as the source for fluid-rich diamonds. *Nature*, *524*(7565), 339–342. https://doi.org/10.1038/nature14857

Wittig, N., Baker, J. A., & Downes, H. (2006). Dating the mantle roots of young continental crust. *Geology*, *34*(4), 237–240. https://doi.org/10.1130/G22135.1

Wu, S., Karius, V., Schmidt, B. C., Simon, K., & Wörner, G. (2018). Comparison of ultrafine powder pellet and flux-free fusion glass for bulk analysis of granitoids by laser ablation-inductively coupled plasma-mass spectrometry. *Geostandards and Geoanalytical Research*, *42*(4), 575–591. https://doi.org/10.1111/ggr.12230

Xu, Y., Li, D., Li, D., Dong, G. C., Pearson, D. G., & Liu, J. (2021). Modification of lithospheric mantle by Melts/Fluids with different sulfur fugacities during the wilson cycle: Insights from Lesvos and global ophiolitic peridotites. *Journal of Geophysical Research: Solid Earth*, *126*(8), e2021JB022445. https://doi.org/10.1029/2021JB022445

Yaxley, G. M., Crawford, A. J., & Green, D. H. (1991). Evidence for carbonatite metasomatism in spinel peridotite xenoliths from western Victoria, Australia. *Earth and Planetary Science Letters*, *107*(2), 305–317. https://doi.org/10.1016/0012-821X(91)90078-V

Zhang, Q., Morel, M. L. A., Liu, J., Legros, H., Luguet, A., Viljoen, K. S., et al. (2022). Re-healing cratonic mantle lithosphere after the world's largest igneous intrusion: Constraints from peridotites erupted by the Premier kimberlite, South Africa. *Earth and Planetary Science Letters*, *598*, 117838. https://doi.org/10.1016/j.epsl.2022.117838

Zhou, S.-H., Shu, Q., Gibson, S. A., Zhang, H.-F., Zhu, J.-J., Legros, H., & Pearson, D. G. (2025). Data for "East meets West: The trace of the Mesoproterozoic Kibaran event in the mantle lithosphere beneath eastern Tanzania" [Dataset]. *Science Data Bank*, *V2*. https://doi.org/10.57760/sciencedb.28397

Zhou, S.-H., Shu, Q., Pearson, D. G., Li, D., Xu, Y., & Liu, J. (2023). Rejuvenation of the lithospheric mantle beneath the orogens: Constraints from elemental geochemistry and Os isotopes in mantle xenoliths. *Geochimica et Cosmochimica Acta*, *349*, 96–114. https://doi.org/10.1016/j.gca.2023.04.006

Zhou, S.-H., Yu, S.-Y., Shu, Q., Chen, L.-M., & Kang, J. (2023). Formation and evolution of lithospheric mantle beneath the Yilan-Yitong fault zone, Northeast China: Constraints from the Shangzhi peridotite xenoliths. *Journal of Asian Earth Sciences*, *254*, 105746. https://doi.org/10.1016/j.jseaes.2023.105746

Zindler, A., & Hart, S. (1986). Chemical geodynamics. *Annual Review of Earth and Planetary Sciences*, *14*(1), 493–571. https://doi.org/10.1146/annurev.ea.14.050186.002425

References From the Supporting Information

Bizzarro, M., Baker, J. A., & Ulfbeck, D. (2003). A new digestion and chemical separation technique for rapid and highly reproducible determination of Lu/Hf and Hf isotope ratios in geological materials by MC-ICP-MS. *Geostandards Newsletter*, *27*(2), 133–145. https://doi.org/10.1111/j.1751-908X.2003.tb00641.x

Blichert-Toft, J., Chauvel, C., & Albarède, F. (1997). Separation of Hf and Lu for high-precision isotope analysis of rock samples by magnetic sector-multiple collector ICP-MS. *Contributions to Mineralogy and Petrology*, *127*(3), 248–260. https://doi.org/10.1007/s004100050278

Blichert-Toft, J. (2001). On the Lu-Hf isotope geochemistry of silicate rocks. *Geostandards Newsletter*, *25*(1), 41–56. https://doi.org/10.1111/j.1751-908X.2001.tb00786.x

Chen, K., Walker, R. J., Rudnick, R. L., Gao, S., Gaschnig, R. M., Puchtel, I. S., et al. (2016). Platinum-group element abundances and Re–Os isotopic systematics of the upper continental crust through time: Evidence from glacial diamictites. *Geochimica et Cosmochimica Acta*, *191*, 1–16. https://doi.org/10.1016/j.gca.2016.07.004

Chu, N. C., Taylor, R. N., Chavagnac, V., Nesbitt, R. W., Boella, R. M., Milton, J. A., et al. (2002). Hf isotope ratio analysis using multi-collector inductively coupled plasma mass spectrometry: An evaluation of isobaric interference corrections. *Journal of Analytical Atomic Spectrometry*, *17*(12), 1567–1574. https://doi.org/10.1039/B206707B

Griffin, W. L., Powell, W. J., Pearson, N. J., & O'Reilly, S. Y. (2008). GLITTER: Data reduction software for laser ablation ICP-MS. In P. Sylvester (Ed.), *Laser ablation ICP-MS in the Earth sciences: Current practices and outstanding issues* (pp. 308–311). https://doi.org/10.3749/9780921294801.app02

Tanaka, T., Togashi, S., Kamioka, H., Amakawa, H., Kagami, H., Hamamoto, T., et al. (2000). JNdi-1: A neodymium isotopic reference in consistency with LaJolla neodymium. *Chemical Geology*, *168*(3–4), 279–281. https://doi.org/10.1016/S0009-2541(00)00198-4

Wu, S., Wörner, G., Jochum, K. P., Stoll, B., Simon, K., & Kronz, A. (2019). The preparation and preliminary characterisation of three synthetic andesite reference glass materials (ARM-1, ARM-2, ARM-3) for in situ microanalysis. *Geostandards and Geoanalytical Research*, *43*(4), 567–584. https://doi.org/10.1111/ggr.12301

Wu, S., Yang, Y., Jochum, K. P., Romer, R. L., Glodny, J., Savov, I. P., et al. (2021). Isotopic compositions (Li-B-Si-O-Mg-Sr-Nd-Hf-Pb) and $Fe^{2+}/\Sigma Fe$ ratios of three synthetic andesite glass reference materials (ARM-1, ARM-2, ARM-3). *Geostandards and Geoanalytical Research*, *45*(4), 719–745. https://doi.org/10.1111/ggr.12399